

The Coma Dust of Comet C/2013 US₁₀ (Catalina) – A Window into Carbon in the Solar System

CHARLES E. WOODWARD,^{1,2} DIANE H. WOODEN,³ DAVID E. HARKER,⁴ MICHAEL S. P. KELLEY,^{5,2} RAY W. RUSSELL,^{6,2}
AND DARYL L. KIM^{6,2}

¹*Minnesota Institute for Astrophysics, University of Minnesota, 116 Church Street SE, Minneapolis, MN 55455, USA*

²*Visiting Astronomer at the Infrared Telescope Facility, which is operated by the University of Hawaii under contract 80HGTR19D0030 with the National Aeronautics and Space Administration.*

³*NASA Ames Research Center, MS 245-3, Moffett Field, CA 94035-0001, USA*

⁴*University of California, San Diego, Center for Astrophysics & Space Sciences,
9500 Gilman Dr. Dept. 0424, La Jolla, CA 92093-0424, USA*

⁵*University of Maryland, Department of Astronomy, College Park, MD 20742-2421, USA*

⁶*The Aerospace Corporation, P.O. Box 92957, M2-266, Los Angeles, CA 90009, USA*

(Received 2020.Aug.23; Revised 2020.Nov.09; Accepted 2020.Nov.11)

Submitted to The Planetary Science Journal

ABSTRACT

Comet C/2013 US₁₀ (Catalina) was an dynamically new Oort cloud comet whose apparition presented a favorable geometry for observations near close Earth approach ($\simeq 0.93$ au) at heliocentric distances $\lesssim 2$ au when insolation and sublimation of volatiles drive maximum activity. Here we present mid-infrared $6.0 \lesssim \lambda(\mu\text{m}) \lesssim 40$ spectrophotometric observations at two temporal epochs from NASA’s Stratospheric Observatory for Infrared Astronomy and the NASA Infrared Telescope Facility that yield an inventory of the refractory materials and their physical characteristics through thermal modeling analysis. The grain composition is dominated by dark dust grains (modeled as amorphous carbon) with a silicate-to-carbon ratio $\lesssim 0.9$, little of crystalline stoichiometry (no distinct $11.2 \mu\text{m}$ feature attributed to Mg-rich crystalline olivine), the submicron grain size distribution peaking at $\simeq 0.6 \mu\text{m}$. The $10 \mu\text{m}$ silicate feature was weak, $\approx 12.8 \pm 0.1\%$ above the local continuum, and the bolometric grain albedo was low ($\lesssim 14\%$). Comet C/2013 US₁₀ (Catalina) is a carbon-rich object. This material, which is well-represented by the optical constants of amorphous carbon is similar to the material that darkens and reddens the surface of comet 67P/Churyumov-Gerasimenko. We argue this material is endemic the nuclei of comets, synthesizing results from the study of *Stardust* samples, interplanetary dust particle investigations and micrometeoritic analyses. The atomic carbon-to-silicate ratio of comet C/2013 US₁₀ (Catalina) and other comets joins a growing body of evidence suggesting the existence of a C/Si gradient in the primitive solar system, providing new insight to planetesimal formation and the distribution of isotopic and compositional gradients extant today.

Keywords: Long period comets (933); Coma dust (2159); Interplanetary dust (821); Astrophysical dust processes (99); Near Infrared astronomy (1093)

1. INTRODUCTION

Traces of primordial materials, and their least-processed products, are to be found in the outermost regions of the solar system in the form of ices of volatile materials (H₂O, CO, CO₂, and other more rare species), and more refractory dust grains. This is the realm of comets. Nevertheless, it is certain that this outer re-

gion beyond the frost line was not entirely “primordial” but was “polluted” with the processed materials from the inner disk, the “hot nebular products,” (Brownlee 2014; Ciesla 2011; Wooden et al. 2007; Harker & Desch 2002), where gas-gas and gas-grain reactions occurred (Gail & Tieloff 2017; Gail 2004, 2002). There is considerable evidence that in the cold regions where cometary material formed, forming comet bodies were “salted” with refractory material processed at much higher temperatures (Zolensky et al. 2006).

Considerable efforts have been expended to characterize the nature of refractory cometary grains to un-

derstand the environment of the early solar system from pebbles to planetesimals to larger bodies (see Poulet et al. 2016, and references therein). These grains likely are minimally processed over the age of the solar system after incorporation into the nuclei of comets. Information on the nature of these grains comes from a variety of sources, including remote sensing through telescopic observations (ground-based, airborne, and space-based), rendezvous/encounter experiments (i.e., *Giotto*, *Rosetta/Philae*, *Deep Impact*), collection of interplanetary dust particles (IDPs) in the Earth’s stratosphere, and a sample return mission (*Stardust*). All these activities have made important contributions to our understanding of these grains. The most detailed information we have comes from the latter two types of studies, where laboratory analysis is possible. Yet, the IDPs from comets 81P/Wild 2 and 26P/Grigg-Skjellerup are vastly different. The former contains material processed at high temperature (Zolensky et al. 2006) while the latter is very “primitive” (Busemann et al. 2009). For these reasons, it is necessary to determine as best we can the properties of dust grains from a large sample of comets using remote techniques (Cochran et al. 2015). These include observations of both the thermal (spectrophotometric) and scattered light (spectrophotometric and polarimetric). The former technique provides our most direct link to the composition (mineral content) of the grains.

With these data, combined with modeling features in the infrared spectral energy distribution (SEDs) arising from mineral species emitting in the comet coma (dust grains) and dynamical models of solar system formation and planetary migration we can address fundamental questions of solar system formation. These questions include: What was the method of transport of these materials, and has information on the scale of those transport processes been stored in primitive solar system objects? Do comets, the remnants of that epoch, still contain clues as to what happened?

In this paper we report our post-perihelion (TP = 2015 Nov 15.721 UT) spectrophotometric observations of comet C/2013 US₁₀ (Catalina), a dynamically new (see Oort 1950, for a definition based on orbital elements) Oort Cloud comet with $1/a_{\text{org}} = 5.3 \times 10^{-6} \text{ AU}^{-1}$ (Williams 2019) and discuss important new interpretations that the coma grain composition of comets from remote sensing observations can bring to understanding disk processing in the primitive solar system.

2. OBSERVATIONS

Infrared and optical observations of C/2013 US₁₀ (Catalina) were conducted at two contemporaneous epochs near close Earth approach ($\Delta \simeq 0.93 \text{ au}$) with the NASA Infrared Telescope Facility (IRTF) and NASA’s Stratospheric Observatory for Infrared Astronomy (SOFIA) facility. Table 1 summarizes the all observational data sets discussed herein and physical parameters of the comet.

2.1. Ground-based Spectrophotometry

Medium resolution ($R \equiv \lambda/\Delta\lambda \simeq 50 - 120$) infrared spectroscopy of comet C/2013 US₁₀ (Catalina) was obtained on the NASA IRTF telescope with The Aerospace Corporation’s Broadband Array Spectrograph System (BASS; Hackwell et al. 1990) during the early morning (daytime) hours. BASS has no moving parts and observes all wavelengths in its 2 to 14 μm operable range using two 58 element block impurity band linear arrays simultaneously through the same aperture. All observations were obtained with a fixed 4''0 diameter circular aperture. Standard infrared observing techniques were employed, using double beam mode with a chop/nod throw of $\simeq 60''$. Sprague et al. (2002) provide a detailed description of the BASS data acquisition and preliminary reduction scheme. Non-sidereal tracking of the comet by the IRTF telescope was performed using Jet Propulsion Laboratory (JPL) Horizons’ (Giorgini et al. 1996) generated rates, and fine guiding, to keep the comet photocenter in the BASS aperture, was done either by manually guiding on the visible comet image produced by the BASS sky-filtered visible CCD camera, or off a strip-chart using thermal channels of the BASS array.

Photometric calibration of individual comet data sets were performed using observations of α Boo observed at equivalent airmass to minimize telluric corrections. α Boo is a well-characterized infrared standard for ground- and space-based telescopes and has been extensively monitored and modeled by the BASS instrument team and other investigators for decades. The calibration and telluric corrections are uncertain to within $\simeq 3\%$. Examination of independent, flux calibrated spectra of comet C/2013 US₁₀ (Catalina) obtained during the course of the 2016 Jan 10.61 UT observational campaign showed no variance in the flux level of the spectral energy distribution (i.e., no outbursts, or jet induced changes in coma brightness were witnessed), or spectral shape. Hence, all spectra were averaged together (with the proper propagation of all statistical point-to-point uncertainties) to produce the final spectrum presented in Fig. 1.

Optical imagery of the comet was obtained on 2016 January 11.633 UT with the NASA IRTF MORIS camera (Gulbis et al. 2011) in a Sloan Digital Sky Survey (SDSS) i' filter ($\lambda_c = 0.7630 \mu\text{m}$, filter full width half maximum (FWHM) of $0.1530 \mu\text{m}$). Multiple exposures

Table 1. Observational Summary – Comet C/2013 US10 (Catalina)^a

Mean		Grism	Single	Total				Tail ^b	Tail ^b
Observation			or	On Source				anti-Sun	anti-velocity
Date	Instrument	Filter	Exposure	Integration	Phase			vector	vector
2016 UT	Configuraion	λ_c	Time	Time	r_h	Δ	Ang	Gas	Dust
(dd-mm hr:min:s)		(μm)	(sec)	(sec)	(AU)	(AU)	($^\circ$)	($^\circ$)	($^\circ$)
<u>NASA SOFIA</u>									
FORCAST (FOF276)									
02-10T07:06:59.6	Imaging SWC	7.70	23.88	477.52	1.710	1.106	32.96	103.54	23.31
02-10T07:29:47.6	Imaging Dual	11.01	18.79	244.28
02-10T07:46:06.4	Imaging Dual	19.70	21.38	171.05
02-10T07:29:47.6	Imaging Dual	31.36	19.29	405.17
02-10T08:01:00.8	Grism SWC	G063	5.00	669.50
FORCAST (FOF275)									
02-09T08:09:02.3	Imaging SWC	7.70	24.90	498.07	1.697	1.080	33.06	106.50	24.80
02-09T08:31:48.8	Imaging Dual	11.01	18.83	131.08
02-09T08:38:42.9	Imaging Dual	11.01	18.83	131.08
02-09T08:46:50.0	Imaging Dual	19.70	20.05	180.49
02-09T08:31:48.8	Imaging Dual	31.36	18.83	131.80
02-09T08:38:42.9	Imaging Dual	31.36	18.83	131.80
02-09T09:07:56.2	Grism LWC	G111	11.82	574.73
02-09T09:52:30.2	Grism LWC	G227	12.00	816.07
02-09T10:34:58.3	Grism LWC	G329	11.97	742.35
<u>NASA IRTF</u>									
MORIS									
01-11T15:11:06.6	Imaging Optical	SDSS i'	5.00	20.00	1.315	0.747	47.80	292.10	157.27
BASS									
01-10T14:34:30.0	IR Spectra	2.6-14.2	960.00	4800.00	1.307	0.758	48.72	293.42	157.37

NOTE—

^aObservation geometry calculated by JPL Horizons (Giorgini et al. 1996).^bVector direction measured CCW (eastward) from celestial north on the plane of the sky.

(5 sec each) of the comet nucleus and surrounding coma were obtained using AB pairs nodding the telescope by 60'', and dithering the telescope while tracking at the non-sidereal rate corresponding to the predicted motion of the comet in an airmass range of ≈ 1.18 . All images were corrected for overscan, and bias with stan-

dard IRAF¹ routines. The data was photometrically calibrated using GSC 02581–02323 (G2V) SDSS colors reported from SIMBAD transformed to the USNO system as described in Tucker et al. (2006), adopting 3631 Jy for zeroth magnitude. No color corrections for spectral type were applied in the transformation. The

¹ IRAF is distributed by the National Optical Astronomy Observatory, which is operated by the Association of Universities for Research in Astronomy (AURA) under cooperative agreement with the National Science Foundation.

average nightly seeing was $\sim 2''.2$ as determined from the standard star. The observed i' flux density of the comet measured in an equivalent BASS aperture was $(2.316 \pm 0.001) \times 10^{-17} \text{ W cm}^{-2} \mu\text{m}^{-1}$.

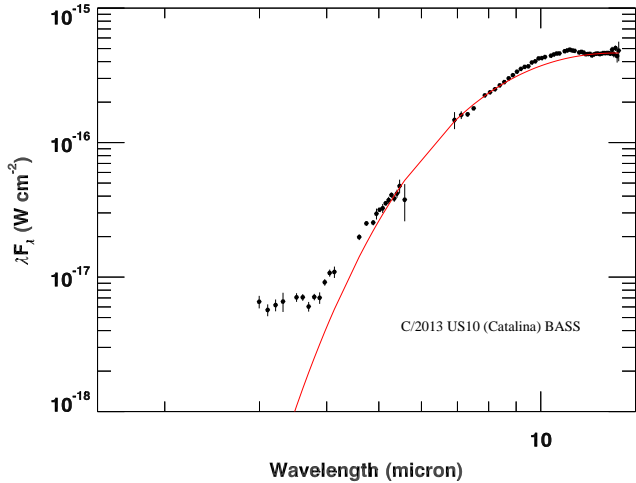


Figure 1. Comet C/2013 US₁₀ (Catalina) 3.0 to 14 μm BASS spectrum obtained on 2016 Jan 10.61 UT with the NASA IRTF telescope. This spectrum was derived by averaging all photometrically calibrated individual comet spectra obtained over a 1.33 hr interval. Regions of poor telluric transmission ($\lesssim 30\%$) where from atmospheric CO₂ and H₂O vapor have strong absorption bands result in gaps in the data where BASS spectral data points are clipped out. The red curve is the best-fit blackbody, $T_{\text{BB}} = 265.3 \pm 2.6 \text{ K}$ fit to the local 10 μm continuum as described in §3.3. The excess over the blackbody curve at short wavelengths is due to scattered, reddened sunlight contributing substantially to the flux.

2.2. Airborne SOFIA Observations

Mid-infrared (mid-IR) spectrophotometric observations of comet C/2013 US₁₀ (Catalina) were obtained using the Faint Object InfraRed CAmera (FORCAST; Herter et al. 2018) mounted at the Nasmyth focus of the 2.5-m telescope of the SOFIA Observatory (Young et al. 2012). FORCAST is a dual-channel mid-IR imager and grism spectrometer operating from 5 to 40 μm .

The data were acquired on two separate, back-to-back flights, originating from Palmdale, CA at altitudes of $\simeq 11.89 \text{ km}$ in 2016 February, conducted as part of our SOFIA comet programs (P.I. Woodward, AOR_ID 04.0010). Mid-infrared imaging observations of C/2013 US₁₀ (Catalina) in three filters and the The Short Wavelength Camera (SWC) grism (G063) were obtained on the first flight, while on the second flight, imaging in the same three filters was repeated in addition to Long Wavelength Camera (LWC) grism observations with three gratings (G111, G227, and G329). For all spectroscopic observations the instrument was

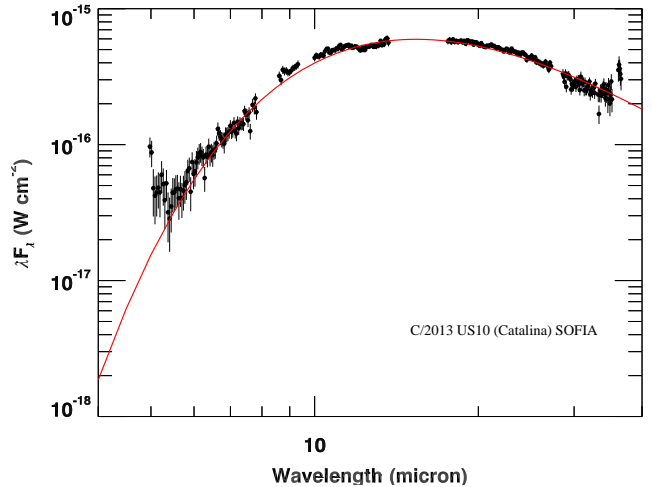


Figure 2. Comet C/2013 US₁₀ (Catalina) composite 4.9 to 36.5 μm FORCAST spectrum obtained with SOFIA on 2016 Feb 09.41 UT (mean UT of both nights). Regions of poor telluric transmission ($\lesssim 70\%$) at flight altitudes result in gaps within certain wavelength intervals within each individual grism where FORCAST spectral data points are clipped out. The red curve is the best-fit blackbody that yields a $T_{\text{BB}} = 239.5 \pm 0.5 \text{ K}$ fit using all wavelengths $\gtrsim 6.0 \mu\text{m}$ as described in §3.3.

configured using a long-slit ($4''.7 \times 191''$) which yields a spectral resolution $R = \lambda/\Delta\lambda \sim 140\text{--}300$. The comet was imaged in the SWC using the F197 filter to position the target in the slit. Both imaging and spectroscopic data were obtained using a 2-point chop/nod in the Nod-Match-Chop (C2N) mode with $45''$ chop and $90''$ nod amplitudes at angles of $30^\circ/210^\circ$ in the equatorial reference frame.

The FORCAST scientific data products were retrieved from the SOFIA archive, after standard pipeline processing and flux calibration was performed (for details see Clarke et al. 2015; Woodward et al. 2015). An extensive discussion of the FORCAST data pipeline can be found in the Guest Investigator Handbook for FORCAST Data Products, Rev. B²

The computed atmospheric transmission at flight altitudes was used to clip-out grism data points in wavelength regions where the transmission was less than 70%. Subsequently, to increase the signal-to-noise (SNR) ratio of the comet spectra, data in each grism spectra segment were binned using a weighted 3-point boxcar. As there is no wavelength overlap between individual FORCAST grism segments, combined with an inherent uncertainty in the absolute grism flux calibration, and the fact that observations were conducted on separate nights, photometry derived from the image data was used to scale

² https://www.sofia.usra.edu/Science/DataProducts/FORCAST_GI_Handbook

the grism data to a common spectral energy distribution (SED). Integration of the observed grism data with the corresponding filter transmission profile lying within the respective grism spectral grasp (i.e., FORF111 for G111) was used to construct a synthetic photometric point. This latter photometric point was compared to the observed image aperture photometry derived within an equivalent circular diameter beam corresponding to the grism extraction aperture area (average for all grisms was $17''.54 \pm 0''.74$, derived data product keyword PS-FRAD). The grism scaling factor was derived from this ratio ($\lesssim 8\%$). Neither the shape of the observed SED inferred from the image photometry nor the relative flux level of the SED changed significantly over the two epoch of the SOFIA observations.

The resultant composite FORCAST spectra of comet C/2013 US₁₀ (Catalina) is presented in Fig. 2. Figure 3 presents panels for each individual grating segment, spanning the respective spectral grasp, to illustrate spectral details of the observed SEDs.

Optical images in the SDSS i' filter also were obtained on each flight series prior to the start of the mid-infrared observing sequence using the Focal Plane Imager (FPI+; Pfüller et al. 2016). The FPI+ field-of-view is 8.7 square arcminutes, with a plate scale of $0''.51$ per pixel, and a FWHM of $\approx 3''.75$. The comet was tracked using the JPL Horizons non-sidereal rates. These data frames were bias and overscanned corrected using standard routines. The comet’s surface brightness was flux calibrated by using aperture photometry of seven stars in the image field of view with known i' magnitudes taken from the USNO UCAC4 catalog to establish the photometric zero point (resultant fractional uncertainty of $\approx 1\%$). The observed i' flux density of the comet measured in an equivalent circular aperture corresponding to the average SOFIA FORCAST grism extraction aperture was $(8.215 \pm 0.009) \times 10^{-17} \text{ W cm}^{-2} \mu\text{m}^{-1}$.

3. DISCUSSION

3.1. SOFIA Imagery and Photometry

Images of comet C/2013 US₁₀ (Catalina) obtained during the 2016 February 09 UT flight are presented in Fig. 4. Examination of the azimuthally averaged radial profiles of the comet in each filter reveals comet C/2103 US₁₀ (Catalina) exhibited extended emission beyond the point-spread function (PSF) of point sources observed with FORCAST under optimal telescope jitter performance in each filter.³ Centroiding on the photocenter of the comet nucleus, photometry in an effective circular aperture of radius 13 pixels, corresponding to $9''.984$, with a background aperture annulus of inner radius 30 pixels ($23''.58$) and outer radius of 60 pixels ($47''.16$) was performed on the Level 3 pipeline co-

added (*COA) image data products using the Aperture Photometry Tool (APT v2.4.7; Laher et al. 2012). The photometric aperture is $\approx 3\times$ the nominal point-source full width half maximum (FWHM), and encompassed the majority of the emission of the comet and coma. Sky-annulus median subtraction (ATP Model B as described in Laher et al. 2012) was used in the computation of the source intensity. The stochastic source intensity uncertainty was computed using a depth of coverage value equivalent to the number of co-added image frames. The calibration factors (and associated uncertainties) applied to the resultant aperture sums were included in the Level 3 data distribution and were derived from the weighted average calibration observations of α Boo.

The resultant SOFIA photometry is presented in Table 2. For the SOFIA epoch of comet C/2013 US₁₀ Catalina, the coma did not appear to have jets or active areas creating discernible coma structures, by our visual examination of the photometric images divided by their azimuthally averaged radial profiles.

3.2. Dust Thermal Models of Infrared Spectra

Infrared spectroscopic observations are fitted with thermal models using standard spectral fitting techniques that minimize χ^2 . Interpreting thermal models enables investigation into fundamental quantities of comet dust populations including: (1) bulk composition; (2) silicate structures of disordered (“amorphous silicates”) and/or crystalline forms (forsterite and enstatite); (3) particle structures and size distributions; and (4) coma *bolometric* albedo. Refractory dust particles are much more robust in maintaining the chemical signatures from the time of formation (see Wooden et al. 2017) than the highly volatile ices as well as semi-refractory organics with limited coma lifetimes (Wooden et al. 2017; Dello Russo et al. 2016). Semi-refractory organics are known to exist through their limited lifetimes in comae, and are presumed to be organics in the dust that are modified while in the coma. These are the so-called ‘distributed sources’, distributed to the coma by the dust particles. The semi-refractory organics are not (yet) observed in thermal IR spectroscopy but rather indirectly by the observed delayed release of molecules such as CO and/or H₂CO as described in Disanti et al. (1999) and Cottin & Fray (2008) or by changes in the color of the scattered light (Tozzi et al. 2004). Polarization properties of particles also are dependent upon organics (Hadamcik et al. 2020). Wooden et al. (2017) and Dello Russo et al. (2016) provide a detailed discussion of semi-refractory organics in cometary comae.

Thermal emission spectroscopy when combined with thermal modeling probes the particle composition from the optical active material in comet coma. A number of approaches have been employed to model the dust thermal emission and study the composition of

³ <http://www.sofia.usra.edu/Science/ObserversHandbook/FORCAST.html>

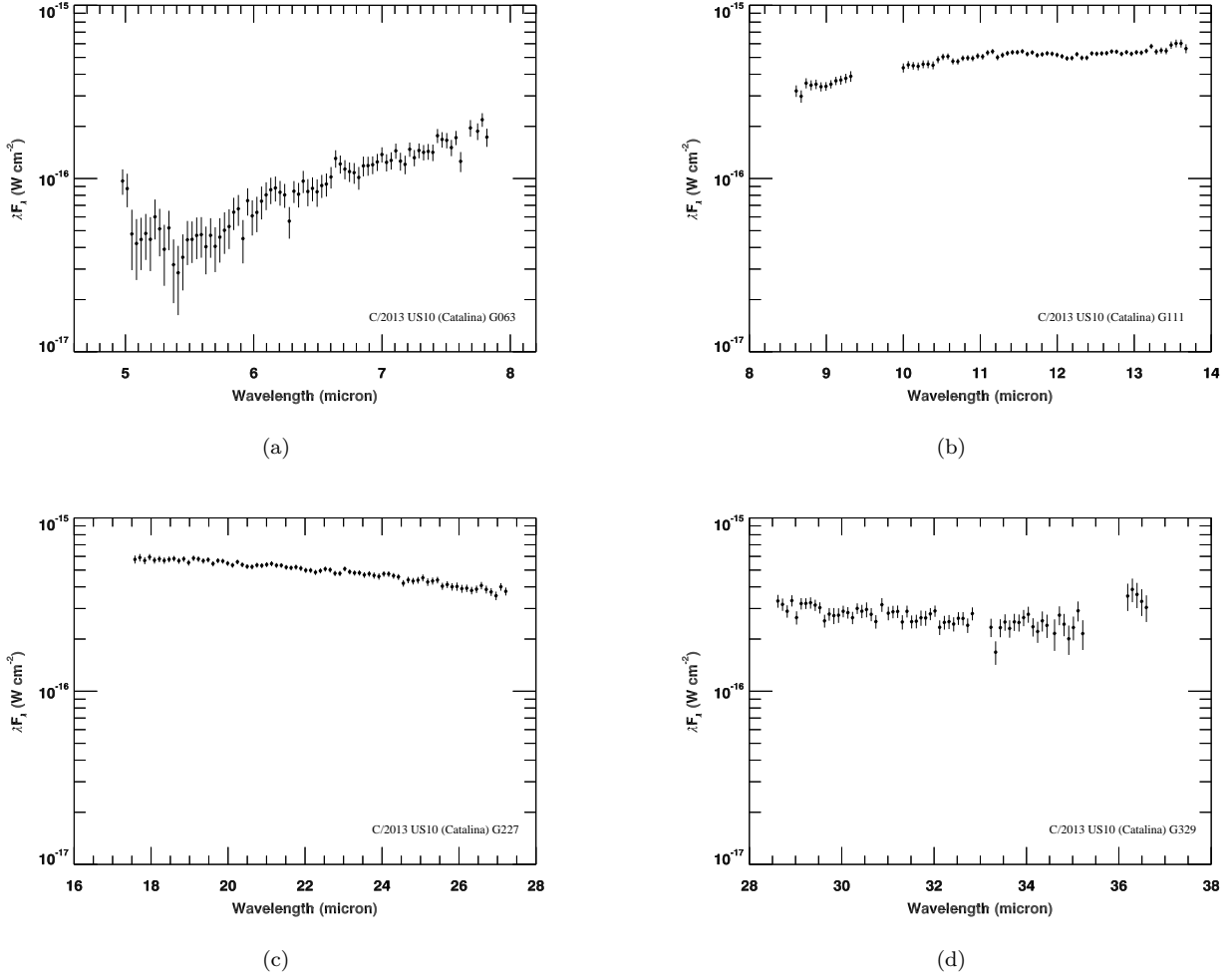


Figure 3. Comet C/2013 US₁₀ (Catalina) SOFIA FORCAST spectra by individual grating to highlight spectral details and the signal-to-noise quality of the data. The panels are (a) G063, (b) G111, (c) G227, and (d) G329. The original spectra have been binned with a 3-point width (in wavelength-space) median boxcar, with the errors propagated by use of a weighted mean. Gaps in the contiguous spectral coverage arise from regions where the atmospheric transmission was modeled to be $\lesssim 70\%$.

cometary particles. Usually, these involve the simultaneous use of a number of different grain compositions (mineralogy), a size distribution, and a description of the particle porosity. Radiative equilibrium is assumed when deriving particle temperatures, which are strongly composition-dependent as well as particle-radius-dependent for low to moderate particle porosities. Particles of more highly absorbing compositions produce higher temperatures and higher flux density thermal emissions. To produce the combined emission of multiple compositions and integrated over grain size distributions, thermal models may employ an ensemble (sums) of individual particles of homogeneous dust materials (Harker et al. 2002, 2011, 2017), or may employ composition “mixtures” calculated using Effective Medium Theory (see Bockelée-Morvan et al. 2017a,b).

At a given heliocentric (r_h [au]) and geocentric (Δ [au]) distance, the particle (dust) composition of the optically

active grains, comprising a linear combination of discrete mineral components, porous amorphous materials, and solid crystals in a comet’s coma can be constrained by non-negative least-squares fitting of the thermal emission model spectra to the observed comet spectrum. The relative mass fractions and their respective correlated errors and the particle properties including the porosity and size distribution, having invoked a Hanner grain-size distribution (HGSD; Hanner 1983) for $n(a)da$, are given as a prescription for the composition of coma particles (for details see Harker et al. 2018, 2011, 2002, and references therein). The particle compositions of dust in the coma of comet C/2013 US₁₀ (Catalina) and relevant parameters from the best-fit thermal modeling are summarized in Table 3. The uncertainties on the derived thermal model parameters reflect the 95% confidence limits that result from 1000 Monte Carlo trials

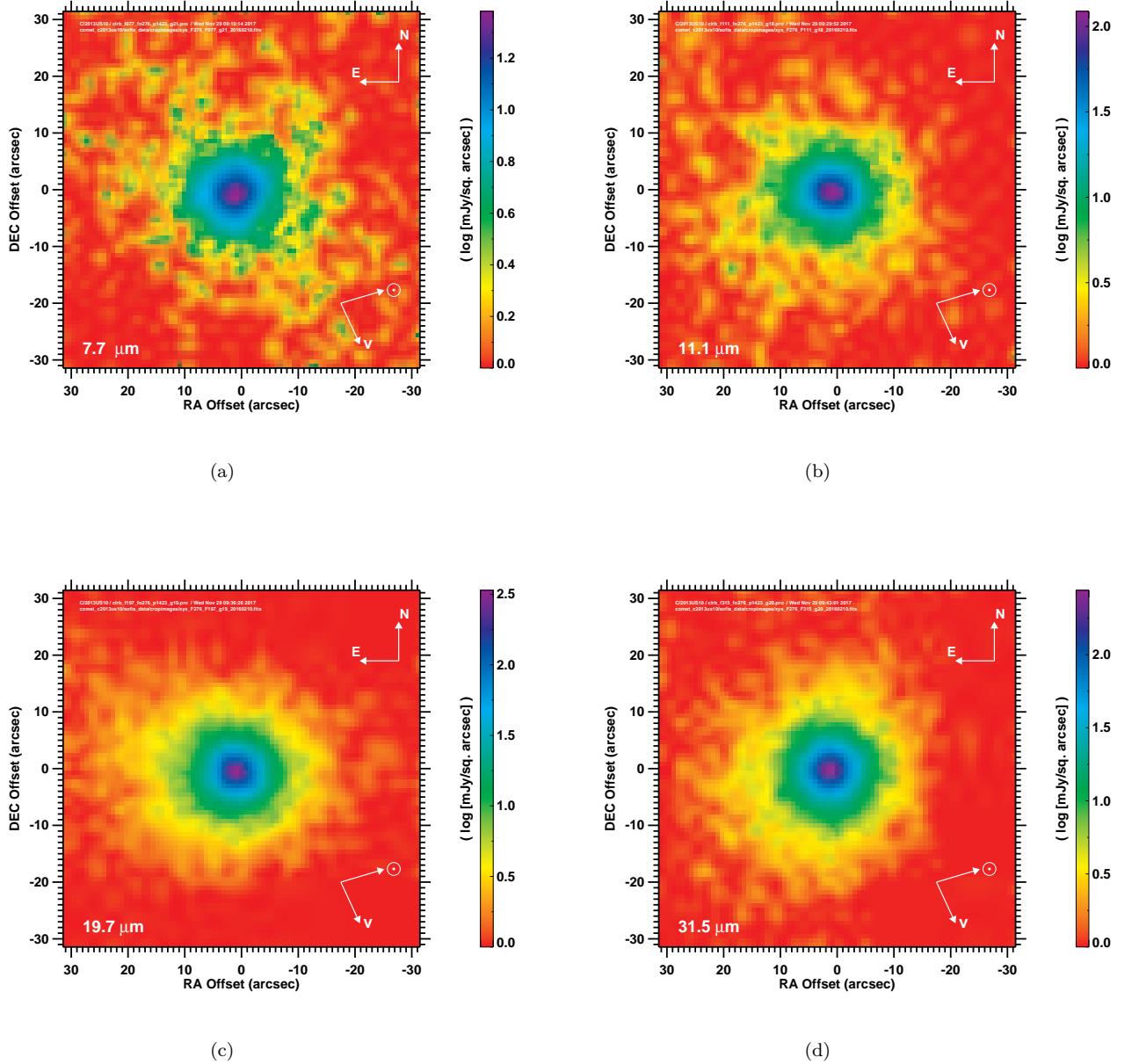


Figure 4. Comet C/2013 US₁₀ (Catalina) FORCAST filter imagery obtained with SOFIA on 2016 February 10.310 UT (mean UT). The images panels are (a) F077 = 7.70 μm ; FWHM = 5''39, (b) F111 = 11.01 μm ; FWHM = 5''23, (c) F197 = 19.70 μm ; FWHM = 4''47, and (d) F315 = 31.36 μm ; FWHM = 4''76. The vector indicating the direction of the comet's motion and the vector indicating the direction toward the Sun are also provided. Images were centroided and shifted using Fourier transform technique to the measured photocenter of the F197 image, and smoothed with a 3-pixel width median boxcar filter.

(Harker et al. 2018). Figures 5 and 6 show the resultant models.

3.2.1. Optical properties and IDP analogues

A particle's composition, structure (crystalline or amorphous), porosity, and effective radius (a) determine its absorption and emission efficiency, Q_{abs} (a grain's absorption efficiency and emission efficiency are equivalent at any given wavelength by Kirchhoff's Law). For an individual particle of effective radius a , $F_{\lambda}(a) \propto$

Table 2. SOFIA Aperture Photometry and $\epsilon f\rho$ of Comet C/2013 US10 (Catalina)

Mean					
Observation					
Date		Fltr	Flux		
UT 2016	InstCfg	λ_c	Density ^a	λF_λ	$\epsilon f\rho$
(dd-mm hr:min:s)	(Imaging)	(μm)	(Jys)	($\times 10^{-16} \text{ W cm}^{-2}$)	(cm)
FORCAST (FOF276)					
02-10T07:06:59.6	SWC	7.70	3.238 ± 0.141	1.261 ± 0.055	7096 ± 308
02-10T07:29:47.6	Dual	11.01	13.8233 ± 0.415	3.767 ± 0.113	7881 ± 236
02-10T07:46:06.4	Dual	19.70	32.467 ± 0.423	4.941 ± 0.064	8522 ± 111
02-10T07:29:47.6	Dual	31.36	29.304 ± 0.303	2.801 ± 0.029	8677 ± 90
FORCAST (FOF275)					
02-09T08:09:02.3	SWC	7.70	3.133 ± 0.459	1.220 ± 0.179	6511 ± 954
02-09T08:31:48.8	Dual	11.01	17.961 ± 0.497	4.855 ± 0.135	9721 ± 271
02-09T08:38:42.9 ^b	Dual	11.01	16.128 ± 0.467	4.390 ± 0.127	8794 ± 255
02-09T08:46:50.0	Dual	19.70	40.100 ± 0.653	6.102 ± 0.099	10159 ± 165
02-09T08:31:48.8	Dual	31.36	34.029 ± 0.809	3.259 ± 0.077	9980 ± 232
02-09T08:38:42.9 ^b	Dual	31.36	36.494 ± 0.575	3.489 ± 0.055	10470 ± 165

NOTE—

^a Measured in a circular aperture with a radius of $17''.664$ centroided on the photocenter of the comet nucleus.^b Aircraft climbing from 12.497 km to 13.106 km during observations.

$\pi \times a^2 \times Q_{\text{abs}}(a) \times B_\lambda(T_{\text{dust}}[a, \text{composition}])$ where B_λ is the Planck blackbody function, evaluated as a function of grain temperature, $T(\text{K})$, particle size, and particle composition (Harker et al. 2002).

Our model uses optical constants (n, k) of five materials (see Harker et al. 2002; Hanner & Zolensky 2010; Wooden et al. 2017, and references therein) to compute $Q_{\text{abs}}(a)$: a Mg-rich crystalline olivine, forsterite with a mineralogy of $(\text{Mg}_y, \text{Fe}_{1-y})_2\text{SiO}_4$, where $0.9 \leq y \leq 1.0$ (Jaeger et al. 1998); a Mg-rich crystalline orthopyroxene, enstatite (MgSiO_3) (Jaeger et al. 1998); amorphous carbon (Edoh 1983),⁴ and amorphous silicates of pyroxene-type and of olivine-type with compositions similar to the stoichiometry of chondritic pyroxene ($\text{Mg}_x, \text{Fe}_{1-x}\text{SiO}_3$ ($x = 0.5$ i.e., Mg:Fe = 50:50) and olivine ($\text{Mg}_y, \text{Fe}_{1-y})_2\text{SiO}_4$ ($y = 0.5$ i.e., Mg:Fe = 50:50) (Dorschner et al. 1995). The amorphous silicates produce the broad width of the the $10 \mu\text{m}$ silicate feature. When present, amorphous pyroxene generates a shorter wavelength shoulder on the $10 \mu\text{m}$ silicate fea-

ture. The crystalline materials are responsible for the sharp peaks in the IR spectra of comets at 11.15 to $11.2 \mu\text{m}$, $19.5 \mu\text{m}$, $23.5 \mu\text{m}$, $27.5 \mu\text{m}$, and $33 \mu\text{m}$ (see Crovisier et al. 1997; Harker et al. 2018). Absence of the latter crystalline spectral features in the observed IR SED does not imply that such species are absent in cometary comae (Harker et al. 2018). However, without detection of spectral features, these species cannot be well-constrained by fitting thermal models to the mid-IR SEDs.

The optical properties of the materials used in the radiative equilibrium calculations for particle temperatures are derived from either laboratory-generated materials or mineral samples from nature. Materials chosen for our thermal models have available optical constants and are found in or are analogous to materials in cometary samples. Crystalline silicates in Interplanetary dust particles (IDPs, Wooden et al. 2000), *Stardust*, UltraCarbonaceous Antarctic MicroMeteorites (UCAMMs; Duprat et al. 2010) are of olivine and pyroxene compositions with a range of Mg:Fe contents with typically $1.0 \leq y \leq 0.5$ and $1.0 \leq x \leq 0.5$ (Wooden et al. 2017; Frank et al. 2014; Joswiak et al. 2014; Dobrică et al. 2012; Brunetto et al. 2011). Only

⁴ Amorphous carbon is used by many modelers (see Bockelée-Morvan et al. 2017a; Rinaldi et al. 2017).

Table 3. Derived Grain Composition of Comet C/2013 US10 (Catalina)^a

Thermal Model SED Details	<u>BASS Spectra^b</u>		<u>SOFIA Spectra^c</u>	
	Relative		Relative	
	Mass		Mass	
	Sub- μm		Sub- μm	
	$(N_p \times 10^{20})^d$	Grains	$(N_p \times 10^{20})^d$	Grains
<u>Dust Components</u>				
Amorphous pyroxene (AP)	$0.132^{+0.014}_{-0.014}$	$0.242^{+0.022}_{-0.023}$	$0.630^{+0.486}_{-0.494}$	$0.174^{+0.119}_{-0.134}$
Amorphous olivine (AO)	$0.029^{+0.007}_{-0.007}$	$0.053^{+0.014}_{-0.013}$	$0.515^{+0.342}_{-0.342}$	$0.142^{+0.115}_{-0.098}$
Amorphous carbon (AC)	$0.567^{+0.003}_{-0.003}$	$0.473^{+0.017}_{-0.015}$	$4.582^{+0.116}_{-0.115}$	$0.574^{+0.083}_{-0.075}$
Crystalline olivine (CO)	$0.072^{+0.009}_{-0.009}$	$0.232^{+0.022}_{-0.024}$	$0.233^{+0.327}_{-0.233}$	$0.111^{+0.123}_{-0.111}$
Crystalline pyroxene (CP)	0.000	0.000	0.000	0.000
<u>Resultants</u>				
Total mass sub- μm grains (gm) $\times 10^8$	$0.942^{+0.030}_{-0.031}$...	$4.853^{+0.745}_{-0.609}$...
Amorphous silicate dust fraction	$0.295^{+0.015}_{-0.014}$...	$0.315^{+0.066}_{-0.067}$...
Crystalline silicate dust fraction	$0.232^{+0.022}_{-0.024}$...	$0.111^{+0.123}_{-0.111}$...
Silicate to Carbon ratio [†]	$1.116^{+0.072}_{-0.074}$...	$0.743^{+0.264}_{-0.220}$...
Crystalline silicate mass to total silicate mass ^e	$0.441^{+0.032}_{-0.035}$...	$0.260^{+0.217}_{-0.260}$...
$a_p(\mu\text{m})^f$	0.7	...	0.5	...
Fractal porosity (D)	2.727	...	2.727	...
<u>Other Parameters</u>				
Hanner Grain-Size Distribution M : N	22.2 : 3.7	...	13.6 : 3.4	...
Reduced χ^2_ν	4.98	...	0.86	...
Degrees of freedom	49	...	168	...

NOTE—

^aUncertainties represent the 95% confidence level.^bComet on 2016 Jan 10 UT $r_h = 1.30$ au, $\Delta = 0.76$ au.^cComet on 2016 Feb 09 UT $r_h = 1.70$ au, $\Delta = 1.09$ au.^dNumber of grains, N_p , at the peak (a_p) of the Hanner grain size distribution (GSD).^e $f_{cryst} \equiv m_{cryst}/[m_{amorphous} + m_{cryst}]$ where m_{cryst} is the mass fraction of submicron crystals.^fPeak grain size (radius) of the Hanner GSD.[†]Ratio represents the bulk mass properties of the materials in the models.

Mg-rich crystalline olivine resonances have thus far been detected definitively in multiple comets using both the mid- and far-IR resonances. Laboratory studies of crystalline olivine by [Koike et al. \(2013\)](#) show that with decreasing Mg-content (i.e., with $y < 0.8$), the $11.2 \mu\text{m}$ peak shifts towards $11.4 \mu\text{m}$ and the far-IR resonances dramatically change to different central wavelengths with different relative intensities. However, these more

fayalitic crystalline olivine resonances have not been detected in comet comae.

Amorphous silicates and amorphous carbon in thermal models are considered candidate ISM or dense cloud materials ([Wooden et al. 2017](#)). The outer cold disk where comet nuclei accreted is a likely reservoir of inherited interstellar grains ([Sterken et al. 2019](#)). However, modeled characteristics of interstellar grains and measured cometary organics differ. [Matrajt et al. \(2005\)](#)

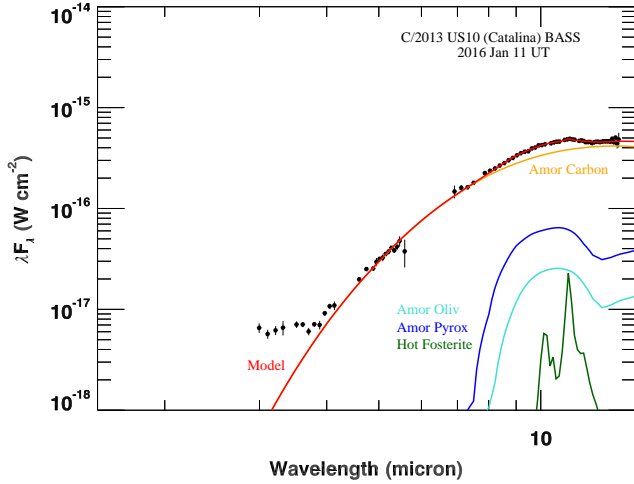


Figure 5. Thermal model spectral energy distribution decomposition of comet C/2013 US₁₀ (Catalina) derived from the 3.0 to 14 μm BASS spectrum obtained on 2016 Jan 10.61 UT at the NASA IRTF telescope. Gaps in the spectra are due to regions of poor telluric transmission within the continuous wavelength range covered by the instrument. The decomposition technique is used to determine the dust composition responsible for the observed coma emission at mid-infrared wavelengths. The solid red line is the best-fit model of the emission from the aggregate dust components, wherein the orange line represent the contribution from amorphous carbon, the dark blue solid line is the emission from amorphous pyroxene, the solid cyan turquoise line depicts the amorphous olivine emission, and the green solid line depicts the crystalline olivine (“hot” forsterite). The observed spectral data are the filled black circles with respective uncertainties. The coma dust composition is dominated by amorphous carbon (dark material) and silicate grains with peak grain sizes (radii) of 0.5 μm (Hanner grain size distribution). Some crystalline material is present.

persistently suggest that the origin of the organic fraction of cometary IDPs is a different environment than the diffuse interstellar medium (DISM) because (a) the 3.4 μm band of organics in anhydrous IDPs is significantly narrower than in the DISM (e.g., towards the Galactic Center that is a mixture of diffuse and dense cloud material) and (b) the aliphatic chains in IDPs are longer (less ramified) than in the DISM, based on the $-\text{CH}_2/-\text{CH}_3$ ratio in IDPs.

The Heterogeneous dust Evolution Model for Interstellar Solids (THEMIS) model (Jones et al. 2017; Jones 2016) predicts the formation and evolution of interstellar dust, from the harsher UV conditions of the ISM, through the DISM, the translucent clouds at the interface of and into dense clouds. In these regimes dust particles eventually either work their way out to less dense phases of the ISM and thus presumably

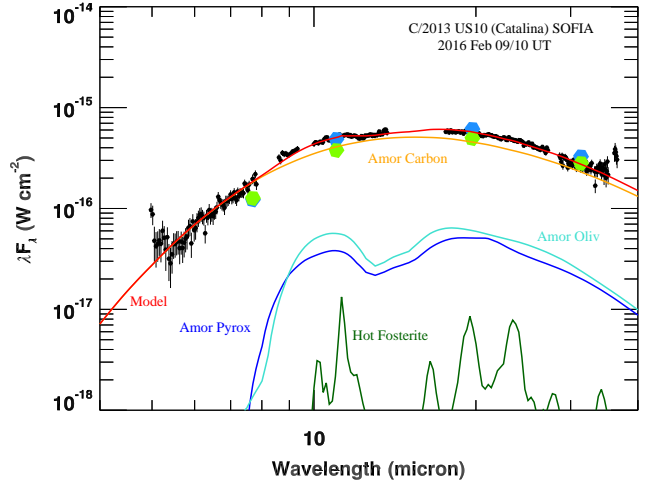


Figure 6. Thermal model spectral energy distribution decomposition of comet C/2013 US₁₀ (Catalina) through all SOFIA grism segments, where the individual components are the same as those described in Fig. 5. The filled blue (2016 February 09 UT) and light green (2016 February 10 UT) circles superposed on the data points (black) are the photometry points taken from the FORCAST imagery in a circular aperture equivalent to the grism extraction area (the average for all grisms was $17''.54 \pm 0''.74$, derived data product keyword PSFRAD) and are used to scale the spectral segments to the photometry. The coma dust composition is dominated by amorphous carbon (dark material) and silicate grains with peak grain sizes (radii) of 0.7 μm (Hanner grain size distribution). Some crystalline material is present.

are cycled into and out of phases, or the dust particles in the dense clouds make their way into protoplanetary disks such as our own. In translucent clouds THEMIS carbon-chemistry facilitates the growth of H-rich and aliphatic-rich matter, denoted a-C(:H), which accretes and then coagulates to tens of nm-size particles through a complex set of chemical reactions. The carbon-chemistry backbones are carbon belt-like molecules with aromatic bonds (n-cyclacenes) and an important process is the epoxylation of the surface materials. The carbonaceous particles, upon return to the harsh UV interstellar radiation field evolve “towards an end-of-the-road H-poor and aromatic-rich a-C material” (Jones & Ysard 2019). Carbonaceous matter in cometary samples appear significantly less dominated by aromatic moieties than implied by THEMIS models. *Stardust* samples only reveal a small concentration of small PAHs (Clemett et al. 2010). Carbon X-ray Absorption Near Edge Spectroscopy (C-XANES) spectra of *Stardust* and IDP organics show saturated aliphatic carbon bonds are more recurrent than aromatic C=C bonds as well as amorphous carbon being the only carbon form common between these samples and Bells, Tagish Lake,

Orgueil and Murchison meteorites (Wirick et al. 2009; De Gregorio et al. 2017). Laboratory absorption spectra do not quantify amorphous carbon as it has no resonances, although its presence can be discerned through Carbon X-ray Absorption Near Edge Spectroscopy (C-XANES; Keller et al. 2004; Messenger et al. 2008).

Amorphous carbon is found in many IDPs (Keller et al. 2004; Busemann et al. 2009; Wirick et al. 2009; Brunetto et al. 2011) but amorphous carbon is not discussed for all IDPs (Flynn et al. 2013; Ishii et al. 2018) nor for all extraterrestrial particulate samples from primitive small bodies, specifically UCAMMs (Dartois et al. 2018; Mathurin et al. 2019). Despite a diversity of bonding structures in cometary organics (Bardyn et al. 2017) as well as organic matter in asteroids, there is a severe paucity of optical constants (de Bergh et al. 2008). Typically, optical constants of relatively transparent tholens are combined with optical constants of the highly absorbing amorphous carbon to darken the models for surfaces of outer ice-rich bodies (de Bergh et al. 2008). Hence, amorphous carbon, which is devoid of aromatic bond IR resonances, is the best choice for the highly absorbing carbonaceous matter in models of dark surfaces of ice-rich bodies as well as for cometary coma particles.

Amorphous silicates in thermal models are analogous to Glass with Embedded Metal and Sulfides (GEMS) in IDPs (see Floss et al. 2006; Brunetto et al. 2011; Bradley 2013; Ishii et al. 2018; Stroud et al. 2019). The ISM silicate absorption feature has spectral similarities to GEMS (Bradley 2013; Stroud et al. 2019) and radiation damage can explain the non-stoichiometry of GEMS (Jäger et al. 2016). An alternative high-temperature formation scenario for GEMS is proposed for the protoplanetary disk (Keller & Messenger 2011) but is challenged by discovery of GEMS with interior organic matter that could not have survived temperatures above 450 K (Ishii et al. 2018). Amorphous silicates are a ubiquitous component of IR spectra of cometary comae and their radiation equilibrium temperatures require compositions of Mg:Fe \approx 50:50 (Harker et al. 2002).

3.2.2. The Hanner Grain Size Distribution (HGSD)

Our modeling invokes the Hanner grain-size distribution $n(a) = (1 - a_0/a)^M (a_0/a)^N$, where a is the particle radius, where $a_0 = 0.1 \mu\text{m}$ is the minimum grain radius, and M and N are independent parameters (Hanner 1983; Hanner et al. 1994). The HGSD is a modified power law that rolls over at particle radii smaller than the *peak* radius $a_p = (M + N)/N$, which is constrained by the thermal model analyses.

3.2.3. Moderately porous particles

The optical properties of porous particles composed of amorphous materials may be calculated by incorporating “vacuum” as one of the material components (Bohren & Huffman 1983). Porous grains are modeled

with an increasing vacuous content as expected for hierarchical aggregation, using the porosity prescription or fractional filled volume given by $f = 1 - (a/0.1 \mu\text{m})^{D-3}$, where a is the effective particle radius, with the fractal dimension parameter D ranging from $D = 3$ (solid) to $D = 2.5$ (fractal porous but still spherical enough to be within the applicability of Mie theory computations; Harker et al. 2018, 2011, 2002, and references therein). Particle porosity affects the observed spectra of comets because the porous grains are cooler than solid grains of equivalent radius as their vacuous inclusions make them less absorbent at UV-visible wavelengths (Harker et al. 2002). The porosity prescription parameter D is coupled with the grain size distribution slope parameter N , and the two parameters are simultaneously constrained when fitting IR SEDs. Increasing porosity (lowering D) decreases particle temperatures, which can be compensated for by increasing the relative numbers of smaller to larger grains by steepening the slope (increasing N) of the HGSD as illustrated in Fig. 2 of Wooden (2002).

An extremely porous particle that is an aggregate of submicron compact monomers can have the same temperature as its monomers ($P(a)_{\text{max}} > 80\%$; Xing & Hanner 1997) or ($P(a)_{\text{max}} \geq 99\%$ with $a \geq 5 \mu\text{m}$; Kolokolova et al. 2007). However, IR spectra of comets are not well-fit by such extremely porous particles that are uniformly as hot as their submicron-radii monomers, regardless of particle size. Thermal models for observed IR spectra of comets need particle size distributions of moderately porous or solid particles. For a comet near 1.5 AU, a HGSD has submicron- to micron-radii particles ($a_{\text{peak}} \leq 1 \mu\text{m}$) that produce the warmer thermal emission under the $10 \mu\text{m}$ silicate feature and at shorter near-IR wavelengths, as well as larger cooler particles producing the decline in the thermal emission at longer (far-IR) wavelengths. Compared to a size distribution of compact solid particles ($D = 3$), a size distribution of moderately porous particles ($P(a) \sim 66$ to 86% , $D = 2.727$ to $D = 2.5$, $a_{\text{eff}} = 5 \mu\text{m}$) are cooler and produce enhanced emission at longer wavelengths while still producing a silicate emission feature with the observed contrast compared to the local “pseudo-continuum” (see § 3.4). Hence, the thermal models constrain the porosity of the amorphous materials (amorphous silicates and amorphous carbon), and the slope and the *peak* radius (a_{peak}) of the grain size distribution of (see Harker et al. 2018, 2011, 2002).

3.2.4. CDE models of solid trirefringent silicate crystals

Silicate crystalline particles are not well modeled as spheres by Mie Theory because of their anisotropic optical constants and irregular shapes (Koike et al. 2010). Crystals are not modeled as porous particles or as mixed-material particles using Effective Medium Theory because modeled resonant features do not match laboratory spectra of the same materials. Discrete solid crystals are better computed using the Continuous Dis-

tribution of Ellipsoids (CDE) approach (Fabian et al. 2001) or the discrete dipole approximation (DDA; Lindsay et al. 2013). Crystals of larger sizes than $\sim 1 \mu\text{m}$ do not replicate the observed SEDs of comets (Min et al. 2005). CDE with c-axis elongated shapes reasonably reproduces laboratory spectra of crystalline forsterite powders (Fabian et al. 2001) and serves as a starting point for our thermal models. Discrete solid crystals with sizes from 0.1 to $1 \mu\text{m}$ are included in our admixture of coma dust materials. From our thermal models, we quote the relative mass fractions for the $\leq 1 \mu\text{m}$ portion of the HGSD in Table 3.

3.2.5. Comet Crystalline Silicates and Disk Transport

The presence of crystalline silicate materials in cometary spectra and in cometary samples indicates transferal of materials that formed in the inner protoplanetary disk to the outer disk (Westphal et al. 2017; Brownlee et al. 2006; Zolensky et al. 2006) where volatile ices (H_2O , CO , CO_2) were extant along with dust particles to become incorporated into cometary nuclei (Rubin et al. 2020). Crystalline silicates are relatively rare along lines-of-sight through the interstellar medium ($\lesssim 5\%$, Kemper et al. 2004) and towards embedded young stellar objects or compact HII regions (1 to 2%, with a few sources at $>3\%$, Do-Duy et al. 2020). A significant crystalline silicate component in cometary dust has been clearly demonstrated by laboratory examinations of *Stardust* (Frank et al. 2014) and IDPs (Brownlee & Joswiak 2017; Busemann et al. 2009; Zolensky & Barrett 1992). Crystalline silicate mass fractions (defined as $f_{\text{crys}} \equiv m_{\text{crys}}/[m_{\text{amorphous}} + m_{\text{crys}}]$ where m_{crys} is the mass fraction of crystals) derived from thermal models of cometary IR SEDs typically are $\sim 20\%$ to 55% (Woodward et al. 2011; Harker et al. 2018, 2011, 2007, 2002; Wooden et al. 2004, and Appendix I). Detailed laboratory studies of cometary forsterite and enstatite crystals show a small fraction have mineralogical signatures of gas-phase condensation such as low iron manganese enriched (LIME) compositions (Joswiak et al. 2017; Frank et al. 2014), ^{16}O -enrichments commensurate with early disk processes (Defouilloy et al. 2018, 2016, 2017), as well as condensation morphologies such as enstatite ribbons in anhydrous IDPs (Bradley et al. 1999).

Moreover, *Stardust* samples and some cluster IDPs contain olivine crystals with a wider range of Fe-contents ($10\% \lesssim \text{Fe} \lesssim 60\%$) than the low Fe-contents of $\simeq 10\%$ to 20% deduced from the wavelengths of the resonances of olivine crystals in cometary spectra (Wooden et al. 2017; Crovisier et al. 1997, 1996). It is a puzzle as to why the spectral signatures of Fe-bearing crystalline silicates are not spectrally detected in comets (Wooden et al. 2017). The Fe-bearing olivine crystals are analogous by their minor element compositions to olivine ($\text{Mg} \leq 80\%$) crystals in type-II chondrules and are called micro-chondrules or chondrule frag-

ments (Brownlee & Joswiak 2017; Frank et al. 2014). In *Stardust* samples, one $15 \mu\text{m}$ -size type-II chondrule called ‘Iris’ has an age-date of ≥ 3 million-years (with respect to CAI formation) and is well-modeled as an isolated igneous system (Gainsforth et al. 2015).

Stardust samples pose a number of challenging questions for disk models about the formation of the nucleus of comet 81P/Wild 2. How did particles radially migrate as late as a few million years in disk evolution to the regime of volatile ices of H_2O , CO and CO_2 ? How did cometary dust minerals that condensed early in disk evolution persist in the disk long enough to be incorporated into this particular cometary nucleus, that is, persist and not be lost via the inward movement of particles? As of yet, satisfactory answers to either of these questions do not exist.

Silicate crystals, specifically referring to forsterite and enstatite that are the abundant Mg-rich silicate crystalline species in comets and/or cometary samples (Wooden et al. 2017), condensed at temperatures near 1800 K or possibly were annealed materials at temperatures near 1100 to 1200 K in shocks (Harker & Desch 2002) under low oxygen fugacity conditions (Wooden et al. 2007). Radial transport may have occurred through a combination of protoplanetary disk processes including advection, diffusion, turbulence and aerodynamic sorting, meridional flows, disk winds, and/or planetary migration (Vokrouhlický et al. 2019; Ciesla 2011; Hughes & Armitage 2010; Wehrstedt & Gail 2008; Gail 2004). Disk models with meridional flows (see Gail 2004) have been successful in predicting $\sim 20\%$ silicate crystalline mass fractions at disk radii of more than tens of AU in <1 million-years.

Radial transport by advection can work through disk wind angular momentum transport (Bai 2016) but can also be produced by turbulent viscosity in the bulk of the disk. Radial transport by diffusion requires turbulence. It is generally thought that magneto-hydrodynamical (MHD) turbulence occurs only in rarified upper layers of the disk atmosphere, if at all (Bai 2016). However even without MHD effects, there are two recently-discussed hydrodynamical mechanisms for producing turbulence: convective over-stability (CO) and vertical shear instability (VSI) that are either individually or collectively operative in various locations in the disk (for example Pfeil & Klahr 2019). Meridional 2D flows are another robust feature of disk models when turbulence mechanisms are considered operative (Lyra & Umurhan 2019; Stoll et al. 2017). Yet, even the qualitative nature of this flow is debated. Meridional flows for 2D and alpha-disk models were outwards along the mid-plane and inwards above one scale height (see Gail 2004). Recent 3D models of meridional flow show that the outward flow is above one scale height so particles that are lofted by turbulence to above one scale height above the mid-plane can move outwards (Pfeil & Klahr 2020;

Stoll et al. 2017). To date, meridional flows only are inferred from ALMA in ^{12}CO observations of the >300 au outer disk regions of the ~ 5 million-year old more massive Herbig Ae/Be system HD 163296 (Teague et al. 2019; Powell et al. 2019). Large scale gas motions are not yet observed for analogs of our protoplanetary disk but cometary crystalline mass fractions suggest inner disk materials moved over large distances.

Models without meridional flows also show outward movement of small particles, merely following the outward advective motion of the gas, at certain radii and times. Estrada et al. (2016) show disk models (see their Fig. 15) with a range of dust particle masses in which the maximum disk radius reached by particles of a specific particle mass (i.e., size) increases with time, i.e., some particles do move outward and the smaller particles are more successful in moving outwards. Porous particles have larger aerodynamic cross sections compared to solid particles of the same mass so porous particles are favored in outward movement compared to solid particles (Estrada & Cuzzi 2016). Ciesla & Sandford (2012) simulate the migration of particles by randomized turbulent ‘kicks’, and thereby nicely illustrate the large-distance motions of some particles.

As a complement to transport within the disk, centrifugally driven disk winds may deposit particles with sizes $\geq 1 \mu\text{m}$ to the outer disk at early times, which “may be relevant to the origin of the $20 \mu\text{m}$ CAI-like particle discovered in one of the samples returned from comet 81P/Wild 2” (Giacalone et al. 2019). Ábrahám et al. (2019) observed the brightest outburst to date from EX Lup using VLTI MIDI interferometry and VLT VISIR IR spectroscopy. Within five years practically all crystalline forsterite that had become enhanced in the inner disk disappeared from the surface of the inner disk. Over that time, the spectral resonances from olivine crystals shifted emphasis from the mid- to far-IR wavelengths indicating that the crystals experienced outward movement.

Disk models are challenged to effectively transport as well as maintain solids in the outer protoplanetary disk against the inward drift of particles, especially as particles grow to ‘pebble’ size and decouple from the gas. Models that treat particle coagulation as well as particle collisional destruction which maintain a population of fine-grained particles (i.e., smaller particles with lower Stokes numbers $[St_\eta]$) then outward movement of small particles with time occurs (see Estrada et al. 2016). Many studies have investigated how material that is injected into the disk spreads outwards and inwards with time (for example, Sengupta 2019). When turbulence is a driving mechanism for radial transport, then aerodynamics affects particle movements, and one can expect signatures of size sorting by $St_\eta \propto \bar{\rho}_s a$, where a is the particle radius and $\bar{\rho}_s$ is the average particle density (Jacquet 2014; Cuzzi et al. 2001). *Stardust* samples demonstrate that aerodynamic sorting in aggregate

formation occurred for particles of olivine compared to FeS, which are denser than olivine (Wozniakiewicz et al. 2013, 2012). The *Rosetta* mission’s imaging studies showed that comet 67P/Churyumov-Gerasimenko’s particles are hierarchical aggregates of hundreds of microns to mm-size with components that are submicron to tens of micron in size (Langevin et al. 2020; Güttler et al. 2019; Hornung et al. 2016). *Stardust* samples and *Rosetta* particle studies are commensurate with the idea that aggregate particle components of submicron to tens of micron of size may be favored over larger solid particles in their outward movement to the disk regimes of comet-nuclei formation.

3.2.6. Revised specific density for Amorphous Carbon

Our thermal model adopts an amorphous carbon (Acar) specific density of $\rho_s(\text{Acar}) = 1.5 \text{ g cm}^{-3}$, from a quoted value of $\rho_s(\text{Acar}) = 1.47 \text{ g cm}^{-3}$ (Williams & Arakawa 1972) measured for the same amorphous carbon material from which our optical constants were derived (Edoh 1983; Hanner et al. 1994).⁵ This specific density of $\rho_s(\text{Acar})$ used in these analyses of comet C/2013 US₁₀ (Catalina) herein represents a significant change from our prior thermal models and publications that used an assumed bulk density of carbon of 2.5 g cm^{-3} (Lisse et al. 1998; Harker et al. 2002), which actually was a specific density slightly higher than that of graphite of 2.2 g cm^{-3} (Robertson 2002). The relative mass fractions of carbonaceous matter and siliceous matter are important and allow us to take a detailed look at the carbonaceous contribution of comets to the hypothesized gradient of carbon in the solar system (§3.9) and as discussed by other authors (Hendrix et al. 2016; Gail & Tieloff 2017; Dartois et al. 2018).⁶

For completeness, in our thermal models the specific density of amorphous silicates is $\rho_s(\text{Asil}) = 3.3 \text{ g cm}^{-3}$ as discussed by Harker et al. (2002, and references therein).

3.3. Coma Dust Composition from Thermal Models

Comet C/2013 US₁₀ (Catalina) is a dynamically new (DN) Oort cloud with eccentricity of $\simeq 1.0003$. Compositionally, the dust in the coma of comet C/2013 US₁₀ (Catalina) is carbon-rich and this comet is among a subset of observed comets that are similarly carbon-rich, some of which are also DN. The carbon-rich dust particles of comet 67P/Churyumov-Gerasimenko were measured *in situ* to have by weight 55% mineral and 45% (carbonaceous) organic (see Fig. 10, Bardyn et al. 2017). If we consider their mineral-to-organic ratio

⁵ Edoh optical constants are of glassy carbon or of an amorphous carbon from the Plessey Company (U. K.) Ltd., Caswell, Towcester, Northants, England (Williams & Arakawa 1972).

⁶ If $\rho_s(\text{Acar}) = 2.5 \text{ g cm}^{-3}$, then comet C/2013 US₁₀ (Catalina) would have yielded C/S ≈ 11 , which is greater than C/Si for any 67P/Churyumov-Gerasimenko particle measured by COSIMA on *Rosetta* (Bardyn et al. 2017).

to be analogous to our silicate-to-carbon ratio then 67P/Churyumov-Gerasimenko has a ratio of 1.1 and C/2013 US₁₀ (Catalina) has ratios of 1.55 and 1.03 for 1.3 au (BASS) and 1.7 au (FORCAST), respectively. However, within the thermal model parameter uncertainties the silicate-to-carbon ratios are the same for both epochs. A decrease by a factor of 1.5 in the silicate-to-carbon ratio for the best-fit values between the two epochs is partly attributed to the definitive detection of crystalline forsterite at 1.3 au that increases the silicate mass fraction relative to the upper limit for forsterite at 1.7 au. Between the two epochs the amorphous carbon increases by a factor of 1.21 (see Table 3).

The dust particle population in comet C/2013 US₁₀ (Catalina) is characterized by a moderate particle porosity ($D = 2.727$). Coma grains extend to submicron size particles, the HGSD (defined in § 3.2.2) peaks at an average $a_p = \{0.7, 0.5\}$ μm , with a grain size distribution slope of $N = \{3.4, 3.7\}$, respectively, for the two epochs at 1.3 au and 1.7 au. The derived coma dust properties of C/2013 US₁₀ (Catalina) share similar characteristics with those found recently for some other long period Oort cloud comets, such as C/2007 N3 (Lulin) which is also DN (Woodward et al. 2011).

The HGSD slope of comet C/2013 US₁₀ (Catalina) is in the range of other comets, including Oort cloud comets, where typically $3.4 \leq N \leq 4$. However, its HGSD slope is greater (steeper) than found for comet 67P/Churyumov-Gerasimenko, which has multiple measurements of its differential grain size distribution $n(a)da$ with slopes of $N = 3.0$ (Bockelée-Morvan et al. 2017a,b), $N = 3.1$ (Rinaldi et al. 2017), $N = 3$ (Della Corte et al. 2019), or $N \simeq 2.7$ to 3.2 for $a < 100$ μm and $N \simeq 1.8$ for $100 \leq a \leq 1000$ μm (Merouane et al. 2016).

Examination of the SEDs of comet C/2013 US₁₀ (Catalina) obtained at two different epoch and the thermal model derived parameters (Table 3) enable us to deconstruct and decipher aspects of the inner coma dust environment (Figs. 5 and 6). From the 58% drop in the available ambient solar radiation between the 1.3 au (BASS epoch) and 1.7 au (SOFIA epoch) observations, one would expect on average the particles on the coma to be cooler at the latter epoch. From the long wavelength shoulder ($\lambda \gtrsim 12.5$ μm) of the 10 μm silicate feature and longward, the SED measured at 1.7 au (Fig. 2) shows enhanced emission at longer wavelengths. Thus, the particles contributing to the far-IR emission are cooler at 1.7 au compared to those at 1.3 au as anticipated. However, the thermal emission at 7.8 μm and bluewards is *similar* for the two epochs. Hence, at 1.7 au the coma of comet C/2013 US₁₀ (Catalina) must have an increased abundance of smaller warm amorphous carbon particles. Moreover, the number of dust particles in the coma at 1.7 au is increased over that at 1.3 au in order to produce about the same flux density of thermal

emission at these two epochs with the cooler particles present at 1.7 au.

There is evidence of a narrow 11.2 μm silicate feature attributable to Mg-rich crystalline olivine (Wooden 2008; Hanner et al. 1994). This is borne out by the detailed thermal modeling of the SED which constrains the relative mass fraction of crystalline forsterite grains in the coma at 1.3 au. The ratio of the crystalline silicate mass to the total silicate mass was ~ 0.44 . The crystalline mass fraction determined for comet C/2013 US₁₀ (Catalina) is greater than that determined for other dynamically new comets such as C/2012 K1 (Pan-STARRS) studied with SOFIA (Woodward et al. 2015). The derived values for each observational epoch are summarized in Table 3.

For the portion of the grain size distribution with radii $a \leq 1$ μm (the submicron population), the silicate-to-carbon ratio is $1.116^{+0.072}_{-0.074}$ and $0.743^{+0.264}_{-0.220}$ at 1.3 au and 1.7 au, respectively (see Table 3). Compared to 1.7 au the higher silicate-to-carbon ratio at 1.3 au is partly due to a factor of ~ 1.25 less amorphous carbon combined with an increase in mass of silicates from the definitive detection of forsterite. This crystalline silicate material produces the sharp peak at 11.1 to 11.2 μm (Koike et al. 2010, and references therein) is relatively transparent outside of its resonances. At 1.3 au, crystalline silicate mass fraction (f_{cryst}) is $0.441^{+0.033}_{-0.035}$ in the coma of comet C/2013 US₁₀ (Catalina) so forsterite crystals contribute significantly to the silicate-to-carbon ratio. Crystalline silicates are tracers of radial migration of inner disk condensates or possibly shocked Mg-rich amorphous olivine so the 44% crystalline mass fraction indicates significant radial transport of inner disk materials out to the comet-forming regime (see §3.2.5).

3.4. Silicate feature shape and strength

The spectral shape of the 10 μm silicate feature can be revealed by dividing the observed flux by a local 10 μm blackbody-fitted ‘pseudo-continuum.’ The shape of the 10 μm silicate feature arises from emission from submicron- to at most several-micron-radii silicate particles in the the coma, depending on the porosity. In thermal models, the ‘pseudo-continuum’ has contributions from porous or solid amorphous carbon, which is featureless at all wavelengths. Thermal models require porous particles ($D = 2.7272$) for comet C/2013 US₁₀ (Catalina). Figure 7 shows the silicate feature shape for comet C/2013 US₁₀ (Catalina) from the BASS observations. The FORCAST mid-IR spectral data show a similar contrast silicate feature but with lower SNR as the BASS data, so these data are not included in the figure for clarity.

The silicate strength parameter historically enables one to inter-compare the dust properties of different comets by quantifying the silicate feature contrast with respect to the local ‘pseudo-continuum’ (Sitko et al. 2004; Woodward et al. 2015). The 10 μm silicate fea-

ture strength, defined as F_{10}/F_c , where F_{10} is the integrated silicate feature flux over a bandwidth of 10 to 11 μm and F_c is that of the local blackbody ‘pseudo-continuum’ at 10.5 μm (Sitko et al. 2004), is a metric that describes the contrast of silicate emission feature. We find the 10 μm silicate feature to be weak in comet C/2013 US₁₀ (Catalina), approximately $12.8\% \pm 0.1\%$ above the local ‘pseudo-continuum.’ The low silicate feature strength in comet C/2013 US₁₀ (Catalina) is similar to some other comets (Sitko et al. 2004, 2013; Woodward et al. 2015, 2011).

A second metric used to compare dust properties of comets is the ratio of the SED color temperature (T_{color}) to the temperature that solid spheres would have at a given heliocentric distance ($r_h(\text{au})$) in radiative equilibrium with the solar insolation, $T_{\text{BB}}(\text{K}) = 1.1 \times 278 (r_h)^{-0.5}$ (see Hanner et al. 1997). At the epoch of the the SOFIA observations, the combined grism 6.0 to 36.5 μm SED can be fit with a single blackbody of temperature 239.5 ± 0.5 K, hence this ratio is $\simeq 1.02$. The enhanced color temperature over a graybody, which is expected for the particles smaller than the wavelength, often is historically referred to as “superheat” S (see Gehrz & Ney 1992). The silicate strength parameter is somewhat correlated to S (Sitko et al. 2004; Woodward et al. 2015). For comet 67P/Churyumov-Gerasimenko, $1.15 \leq S \leq 1.2$, and S is plotted along with the bolometric albedo at phase angle 90° (0.05 to 0.15) and the dust color (% per 100 nm) (Bockelée-Morvan et al. 2019). Comet C/2013 US₁₀ (Catalina) has a smaller value for S than comet 67P/Churyumov-Gerasimenko.

C/2013 US₁₀ (Catalina) and 67P/Churyumov-Gerasimenko, both exhibiting a weak silicate feature and are carbon-rich as determined from thermal modeling, provide a direct contradiction to older concepts commonly asserted in the literature. Commonly, many groups argued that some comets totally lacked silicate features because their solid grains were radiating as graybodies and not displaying resonances because the grains were so large that the grains themselves were optically thick (A’Hearn et al. 2005; Lisse et al. 2005). For comets with low dust production rates, estimation and subtraction of the nucleus’ contribution to the SED is important. When combined with higher sensitivity observations and subtraction of the nucleus flux density, thermal models that integrate over a size distribution of particles with composition-dependent-dust-temperatures shows that the comets with comae particles whose HGSD has $a_p \leq 1$ μm and that display weak silicate features are carbon-rich.

3.4.1. The “Hot crystal model” and SOFIA in the far-IR

The SOFIA spectrum has enhanced emission that rises near 36 μm but the observations do not extend to longer wavelengths to show a decline in flux density. Laboratory absorption spectra of powders of pure-Mg

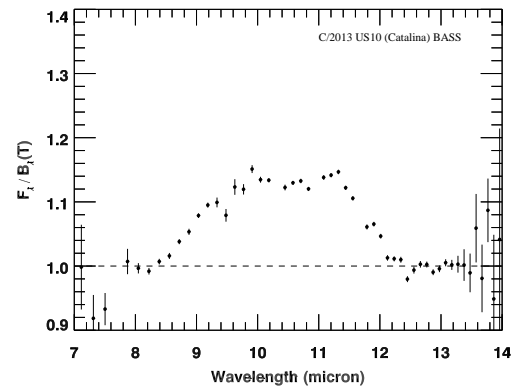


Figure 7. Observed BASS flux density divided by a 265.3 K blackbody continuum derived from the local 10 μm ‘pseudo-continuum’ as defined by Sitko et al. (2004) to highlight spectral details of the 10 μm silicate feature.

forsterite show that the absorbance is about equal at 33 μm and 11.1 μm (Koike et al. 2013), while the 19.5 and 23.5 μm features also having significant absorbance. The 33 μm emission from pure-Mg forsterite (Fo100) is not detected in the far-IR. The slope of the HGSD is well constrained by the SOFIA data (given the low χ^2_ν).

The SOFIA data provide important constraints on the crystalline resonances in the far-IR and on the slope of the HGSD (§3.2.2). Our thermal models employ a “hot crystal model” for the temperatures for forsterite and enstatite, where their radiative equilibrium temperatures of crystals are increased by a factor of 1.9 ± 0.1 based on fitting the *ISO SWS* spectrum of comet C/1995 O1 (Hale-Bopp) (Harker et al. 2002). We speculate that hotter crystal temperatures may arise from crystals being in contact with other minerals that are more absorptive or from Fe metal inclusions such as “dusty olivines” (Kracher et al. 1984), or “relict” grains (Ruzicka et al. 2017).

3.5. Other mineral species not detected

Within our SNR in the SOFIA mid- to far-IR SED, neither hydrated phyllosilicates that have far-IR resonances distinct from anhydrous amorphous olivine and amorphous pyroxene nor the very broad 23 μm troilite (FeS, submicron-sized) (Keller et al. 2002) spectral signatures were seen (see Schambeau et al. 2015). Phyllosilicates, such as Montmorillonite, as well as carbonates have absorptions in the 5 to 8 μm wavelength region (Roush et al. 1991; Crovisier & Bockelée-Morvan 2008) and neither of these compositions were detected in comet C/2013 US₁₀ (Catalina).

3.6. The search for aliphatic and aromatic carbon

The BASS spectrum spans the 3.0 to 3.5 μm wavelength region where potentially the 3.28 μm peripheral hydrogen stretch on a ring carbon macromolecule (PAH)

and the $3.4\ \mu\text{m}$ $-\text{CH}_2$, $-\text{CH}_3$ aliphatic bonds arrangements that are prevalent in IDPs and *Stardust* materials (Matrajt et al. 2013) might be detectable. The analyses of a well-defined aliphatic carbon $3.4\ \mu\text{m}$ band on nucleus surface of 67P/Churyumov-Gerasimenko is presented by Raponi et al. (2020) and Rinaldi et al. (2017) also argue for the presence for this feature in coma observations. The BASS spectrum spans the 3.0 to $3.5\ \mu\text{m}$ wavelength region where potentially the $3.28\ \mu\text{m}$ peripheral hydrogen stretch on a ring carbon macromolecule (PAH) and the $3.4\ \mu\text{m}$ $-\text{CH}_2$, $-\text{CH}_3$ aliphatic bonds arrangements that are prevalent in IDPs and *Stardust* materials (Matrajt et al. 2013) might be detectable. The analyses of a well-defined aliphatic carbon $3.4\ \mu\text{m}$ band on nucleus surface of 67P/Churyumov-Gerasimenko is presented by Raponi et al. (2020) and Rinaldi et al. (2017) also argue for the presence for this feature in coma observations. A broad 20% deep $3.2\ \mu\text{m}$ features from organic ammonium salts also is discussed for the nucleus Poch et al. (2020). If the aliphatic material in comets is similar to that of IDPs then laboratory absorption spectra by (Matrajt et al. 2005) of whole IDPs provide important information on the relative column densities of C atoms participating in different organic bonding groups including aliphatic bonds ($-\text{CH}_2$, $-\text{CH}_3$), aromatic ($\text{C}=\text{C}$), carbonyl and carboxylic acid bonds in ketones, and ammonium salts.

Protopapa et al. (2018) point to the possible presence of an organic emission feature near $3.3\ \mu\text{m}$ in higher spectral resolution observations of comet C/2013 US₁₀ (Catalina) obtained on 2016 January 12 ($r_h = +1.3$ au) but do pursue any further detailed analyses. However, there are strong molecular ro-vibrational emission lines of C_2H_6 and CH_3OH in the 3.28 to $3.5\ \mu\text{m}$ region that significantly complicate deciphering underlying solid state organic features (Bockelée-Morvan et al. 1995; Dello Russo et al. 2006; Yang et al. 2009; Bockelée-Morvan et al. 2017a). Given these challenges, we do not report on detection of any aromatic or aliphatic features in the BASS data at our resolving power and sensitivity for comet C/2013 US₁₀ (Catalina). Thus, no spectral features were seen to indicate the presence of aromatic hydrocarbons (such as HACs, PAHs, a-C(:H) nano-particles) or aliphatic carbons in the coma of C/2013 US₁₀ (Catalina).

Comet C/2013 US₁₀ (Catalina) has one of the few reported 5 to $8\ \mu\text{m}$ wavelength spectrum from SOFIA (+FORCAST). We searched for spectral signatures of vibration modes of $\text{C}=\text{C}$ bonds ($6.25\ \mu\text{m} = 1600\ \text{cm}^{-1}$), based on a constrained search of the observed absorption features in laboratory studies of cometary-like polyaromatic organics in IDPs (Matrajt et al. 2005) and in the UCAMMs (Dartois et al. 2018) as well as asteroid insoluble organic materials (IOM, Alexander et al. 2017). The $6.25\ \mu\text{m}$ $\text{C}=\text{C}$ resonances are not dependent on the degree hydrogenation or the number of peripheral hydrogen bonds compared to structural $\text{C}=\text{C}$

bonds (Keller et al. 2004). The UCAMMs are mass-dominated by organics, richer in N and poorer in O than with probable origins in the outer protoplanetary disk (Dobrica et al. 2009). We also searched for $\text{C}=\text{O}$ bonds ($5.85\ \mu\text{m} = 1710\ \text{cm}^{-1}$). There are tantalizing $\leq 3\ \sigma$ fluctuations near $1620\ \text{cm}^{-1}$ and $1510\ \text{cm}^{-1}$ that are in the regions of $\text{C}=\text{C}$ stretching modes (see Table 2 of Merouane et al. 2014). However, the SNR is insufficient and the width of the fluctuations are narrow, narrower than the widths of the $\text{C}=\text{C}$ resonances in the UCAMMs that have a preponderance of organics such that their features dominate the 5 to $8\ \mu\text{m}$ region.

The lack of resonances from organics in the 5 to $8\ \mu\text{m}$ wavelength region does not discourage us from further searches in cometary comae for these bonding structures with the much higher sensitivity provided by the James Webb Space Telescope (JWST) and its instruments.

3.7. Carbon and Dark Particles

We find amorphous carbon dominates the composition of grain materials in comet C/2013 US₁₀ (Catalina). Dominance of carbon as a coma grain species was seen in other ecliptic comets including 103P/Hartley 2 (Harker et al. 2018) as well as the Oort cloud comets C/2007 N3 (Lulin) (Woodward et al. 2011) and C/2001 HT50 (Kelley et al. 2006). The outburst of dusty material from comet 67P/Churyumov-Gerasimenko at 1.3 au was carbon-only-grains (with radii of order $0.1\ \mu\text{m}$), as measured by VIRTIS-H (Bardyn et al. 2017) and VIRTIS-M (Rinaldi et al. 2018) on *Rosetta*. Comets can exhibit changes in their silicate-to-carbon ratio between observations epochs and notably a few comets have had significant changes in their inner comae silicate-to-carbon ratios during a night's observations (C/2001 Q4 (NEAT) Wooden et al. 2004), (103P/Hartley 2 Harker et al. 2018), (9P/Tempel 1 Harker et al. 2007; Sugita et al. 2005).

Our cometary comae dust atomic C/Si ratios are calculated using a number of suppositions and should be taken as indicative values. Cometary atomic C/Si ratios are of interest for comparison with *in situ* studies of 67P/Churyumov-Gerasimenko and 1P/Halley and of laboratory investigations of IDPs and UCAMMs. The IDPs and UCAMMs are extraterrestrial materials likely to have originated from primitive bodies like comets and KBOs, respectively (Bergin et al. 2015; Dartois et al. 2018; Burkhardt et al. 2019, and references therein). We choose to compare C/Si of the submicron grain component determined from thermal models with bulk elemental composition measurements of IDPs (X-ray measurements). We elect to not compare C/Si ratios derived from resonances (aliphatic $3.4\ \mu\text{m}$, aromatic $6.2\ \mu\text{m}$, and other bond in UCAMMs) because in laboratory baseline-corrected absorption spectra the amorphous carbon component would not be counted because it does not have a resonance.

3.7.1. Endemic Carbonaceous Matter in Comets

A dark refractory carbonaceous material darkens and reddens the surface of the nucleus of 67P/Churyumov-Gerasimenko, the surface material also displays a $3.4\ \mu\text{m}$ (Raponi et al. 2020) and a similar aliphatic feature is suggested to exist in the coma of 67P/Churyumov-Gerasimenko (Rinaldi et al. 2017). We posit that the optical properties of amorphous carbon are representing well the dark refractory carbonaceous dust component observed in cometary comae through IR spectroscopy. Likely this dark refractory carbonaceous material is endemic to the comet’s surface. Cosmic rays of a few 10 keV only damage a thin veneer of hundreds of nm of thickness (Strazzulla et al. 2003; Moroz et al. 2004; Quirico et al. 2016). This damage effects the structure (amorphization) and the composition (destruction of C-H and O-H bonds by dehydrogenation) of the materials (Moroz et al. 2004; Lantz et al. 2015; Quirico et al. 2016). Typical particle radii on the nucleus surface of 67P/Churyumov-Gerasimenko is at least tens of microns based on the observed the red color of the surface at visible wavelengths (Jost et al. 2017), so cosmic rays do not damage the full particle volume. For example, IDPs studied by IR spectra indicate aliphatic bonds in particle interiors (Matrajt et al. 2005, 2013; Flynn et al. 2015) but a lack of organic bonds in their near-surfaces possibly due to damaging ultraviolet light and particle radiation in space (Flynn et al. 2004). Lastly, if the redeposition timescales for particles lofted from the nucleus but not escaping its gravity are about the orbital period of comet 67P/Churyumov-Gerasimenko (Marschall et al. 2020) then the ion-irradiation timescales on the surface, which have been shown to amorphize carbon bonds or damage silicates, are too short by orders of magnitude (Baratta et al. 2004; Brunetto et al. 2014; Quirico et al. 2016).

However, the surface properties of the DN comet like C/2103 US₁₀ (Catalina) may differ from the Jupiter-family comet like 67P/Churyumov-Gerasimenko. A photon penetration depth of $1\ \mu\text{m}$ for cosmic-rays can induce chemical changes, such as development of an organic crust due to the conversion of low molecular weight hydrocarbons into a web of bound molecular species, from electronic ionization in dose time per 100eV per 16-amu (H_2O) in the Local Interstellar Medium, which is a harsher environment than within the heliopause at $\sim 85\ \text{au}$ (see discussion in Strazzulla et al. 2003). Comet C/2013 US₁₀ (Catalina) may have had a radiation damaged dust rime of up to a few cm depth, but DN comets can have their onset of activity at large heliocentric distances (Meech et al. 2009) where likely this material is shed when the comet’s activity first turns on. Thus, the amorphous carbon is not from a radiation rime because of the insufficient volume of the nucleus that can be altered by radiation compared to the mass loss pre-perihelion. Coupled with the arguments about in-

sufficient time scales for materials recently exposed on cometary surfaces from either erosion or re-deposition to be space weathered, we assert that the amorphous carbon that is in the observed comae of comet C/2013 US₁₀ (Catalina) is carbonaceous matter is endemic to the comet nucleus. Moreover, the fluence and time scales or temperatures that change carbon bonding structures typically are not reached in cometary comae. The material is refractory and stable. The dark refractory carbonaceous matter that is modeled with the optical constants of amorphous carbon (see § 3.2.1) is endemic to comets. By the ubiquitous detection of a warm particle component in all cometary IR spectra observed to date, the carbonaceous matter is endemic to comets in general.

If dark refractory carbonaceous matter is stable on the surface then this implies the matter will be stable in the coma, unless the temperatures are raised significantly. For example if the size distribution significantly changes to smaller sizes the latter would occur. Laboratory experiments demonstrate that amorphous carbon becomes graphitized at $\sim 3000\ \text{K}$ (De Gregorio et al. 2017). Comae dust temperatures remain at $\lesssim 400\ \text{K}$ dust compositions and particle sizes near $1\ \mu\text{m}$ -radii for comets near 1 au. The exception will be sun-grazers that come close or enter the solar corona. On the other hand, aliphatic carbon may survive temperatures as high as $\simeq 823\ \text{K}$ if associated with porous minerals (Wirick et al. 2009). In the outburst of 67P/Churyumov-Gerasimenko at 1.3 au, comae dust temperatures reached 550 to 600 K and were modeled by tiny $0.1\ \mu\text{m}$ -radii amorphous carbon particles (Bockelée-Morvan et al. 2019, 2017b; Rinaldi et al. 2018). Thus, comet comae dust particles do not reach such high temperatures as $\simeq 823\ \text{K}$ to destroy aliphatic carbon when comets are near 1 au.

The contribution of amorphous carbon is variable between comets. In some comets, the contribution of amorphous carbon is temporally variable: 103P/Hartley 2 (Harker et al. 2018), C/2001 Q4 (NEAT) (Wooden et al. 2004), and the after the kinetic-impactor encounter in inner coma of 9P/Tempel 2 (Sugita et al. 2005; Harker et al. 2007). The variability of amorphous carbon between comets and the temporally variability for a few comets gives clues to the diversity of protoplanetary disk reservoirs out of which comet nuclei formed. The variability in silicate-to-amorphous carbon ratios for an individual comet also may be related to the size sales of variable-compositions of the nucleus (Belton et al. 2007), to jets (Wooden et al. 2004), or variations coupled to changes in solar insolation in different parts of comets orbits (seasonal effects; Combi et al. 2020). These variations asserted for the nucleus are tied to the hypothesis that the refractory dust particle compositions observed in the coma are endemic to the comet.

3.8. Amorphous carbon and other forms of carbon

Amorphous carbon is the one carbon bonding structure common to IDPs, Stardust, and four carbonaceous chondrites including Bells, Tagish Lake, Orgueil, and Murchison (Wirick et al. 2009; De Gregorio et al. 2017). The amorphous carbon bonding structure is observed specifically through C-XANES (Matrajt et al. 2008a) and in *Stardust* particles from comet 81P/Wild 2 (Matrajt et al. 2008b). In addition to C-XANES spectra, regions of some IDPs are described as poorly graphitized or highly disordered carbon (Thomas et al. 1993b,a).

Other organic bonding structures besides amorphous carbon that are found in cometary samples (IDPs and *Stardust*) are: aliphatic, aromatic, and rarely graphitic. IDP organic matter generally occurs as aliphatic-dominated rims (Flynn 2008; Flynn et al. 2015), rims on mineral grains with aromatic (C=C) and carbonyl group (C=O) bonds (Flynn et al. 2013), (non-graphitized) aliphatic or aromatic macromolecular material (De Gregorio et al. 2017) as submicron-sized pieces associated with mineral crystals (Wirick et al. 2009), or as a matrix (Brunetto et al. 2014). In one IDP, different bonding structures of carbon occurs in micron-sized regions and where amorphous carbon was mixed with GEMS (Brunetto et al. 2014). Two IDPs show N-rich organic rims on GEMS that are in turn are inside other GEMS, indicating two formation epochs, and their specific organic matter requires particle temperatures remained cooler than ~ 450 K (Ishii et al. 2018). Cometary carbonaceous matter is sometimes referred to as polyaromatic when there are significant moieties of aromatic C=C bonds. UCAMMs are noted for abundant aromatic material as well as for their N=C and N-C bonds (Dartois et al. 2018; Mathurin et al. 2019).

Only four cometary samples display graphitic carbon bonding structures as witnessed through C-XANES. Two of these are from *Stardust* samples, seen as halos on Fe grain cores which are hypothesized to have formed at high temperatures and at low oxygen fugacity in the protoplanetary disk (De Gregorio et al. 2017), and in two IDPs (L2021C5, L2021Q3) where its close proximity to other bonding structures is discussed respectively by Brunetto et al. (2014) and (L2021Q3 Merouane et al. 2016). Graphite can be formed at high temperatures ($\gtrsim 3273$ K) although there are lower temperature processes that form graphite (Wirick et al. 2009). Ion bombardment of amorphous carbon is a competing process between amorphization and graphitization and this process depends on the structure of the starting amorphous carbon (Brunetto et al. 2011). Raman spectroscopy of one IDP shows “localized micrometer-scale distributions of extremely disordered and ordered carbons” (Brunetto et al. 2011).

In summary, cometary carbonaceous matter is macromolecular (De Gregorio et al. 2017) and not strictly aromatic (containing aromatic bonds) like meteoritic IOM

(Alexander et al. 2007), as well as highly variable in composition and structure.

3.9. Cometary comae elemental C/Si ratios

In the following discussion, we investigate the plausible implications of cometary comae thermal model’s relative mass fractions (i.e., the mass fraction of amorphous carbon to the mass fractions of the amorphous and crystalline silicates) on the elemental abundance ratio of C/Si. We compare inferred elemental ratio C/Si for comet C/2013 US₁₀ (Catalina) from thermal models to the C/Si ratio determined for IDPs using Scanning Electronic Microscopy with Energy Dispersive X-ray analysis (the SEM-EDX method, Thomas et al. 1993b), and by mass spectrometry for comet 1P/Halley, and comet 67P/Churyumov-Gerasimenko (COSIMA).

We will show that the relative mass fractions of C/Si derived from our thermal models of comet C/2013 US₁₀ (Catalina) and a handful of other recently observed and modeled comets are consistent with the average $C/Si = 5.5^{+1.4}_{-1.2}$ derived by COSMIA for thirty 67P/Churyumov-Gerasimenko particles (Bardyn et al. 2017), for 1P/Halley particles measured by Vega-1 and Vega-2 mass spectrometers during spacecraft encounters, and also for the upper range of C/Si for IDPs (see Bergin et al. 2015). The enigmatic comet C/1995 O1 (Hale-Bopp) with its propensity of submicron crystalline silicates (Harker et al. 2002) also is included in our analysis to demonstrate its lower C/Si ratio that is in the lower range of the IDP C/Si ratios (Bardyn et al. 2017) and also close to the range determined for CI chondrites (Bergin et al. 2015).

Our cometary comae dust C/Si atomic ratios are calculated using a few suppositions and should be taken as indicative values, which are of interest for comparison with *in situ* studies of 67P/Churyumov-Gerasimenko and 1P/Halley and of laboratory investigations of IDPs and UCAMMs (Matrajt et al. 2005; Brunetto et al. 2014; Bardyn et al. 2017; Dartois et al. 2018). The IDPs and UCAMMs are extraterrestrial materials likely to have originated from primitive bodies like comets and KBOs, respectively (Dobrica et al. 2009, and references therein). Unlike laboratory measurements of IDPs, micrometeoritic samples, or *Stardust* particles which generally are the measure of single grains or isolated domains within a matrix, values returned from remote-sensing spectroscopic observations represent a coma-wide measure from a large ensemble of thermally radiating dust particles of various radii.

Our suppositions in deriving C/Si atomic ratios are: (a) amorphous carbon is a good optical analog for dark highly absorbing carbonaceous matter in cometary comae and (b) thermal model relative mass fractions derived for amorphous carbon are representing a significant fraction of the carbonaceous matter in the coma §3.9.1.

3.9.1. Counting Carbon Atoms

We are comparing the C/Si atomic ratio derived for cometary samples using different techniques. Mass spectroscopy directly measures the elemental C/Si ratio, which is the method for *in situ* measurements. However, non-destructive techniques that allow counting the carbon atoms in IDPs or *Stardust* samples depend on the method. X-ray SEM-EDX techniques (Thomas et al. 1993b) can count all the carbon atoms whereas IR absorption spectroscopy counts the carbon atoms involved in the observed resonances. Laboratory IR absorption spectroscopy measures the C/Si by converting the integrated band strengths into the number of atoms for aliphatic and/or aromatic bands compared to the 10 μm silicate band (Matrajt et al. 2005; Brunetto et al. 2014). Laboratory absorbance spectroscopy fits and subtracts a spline baseline to yield a linear baseline for the purpose of integrating the observed band strengths (see Matrajt et al. 2005). Amorphous carbon is not observed in absorbance in spectroscopy of IDPs because amorphous carbon lacks spectral resonances. To make a comparison between cometary C/Si derived from thermal models of amorphous carbon and C/Si derived from laboratory measurements and *in situ* measurements, we choose to employ the SEM-EDX measurements that are counting the carbon atoms but not discerning the carbon bonding structures.

Currently we cannot claim knowledge of aliphatic and aromatic content in comet comae dust populations of multiple comets via IR spectroscopy. If we cannot detect signatures of these bonding structures, we cannot definitely determine their contribution to the observed emission. However, we can use IDPs to indicate what the potential increase in C/Si might be if the aliphatic or aromatic bonds were spectroscopically detected.

We can examine what C/Si atomic ratios are derived from organic features in laboratory absorbance spectra of IDPs and compare to the C/Si derived for comets using thermal modeling of the warm particle component that is modeled with amorphous carbon. Many IDPs show the aliphatic 3.4 μm feature. The 3.4 μm feature is composed of the aliphatic CH_2 symmetric vibration (at $\sim 2850 \text{ cm}^{-1}$), the CH_2 asymmetric vibration (at $\sim 2922 \text{ cm}^{-1}$) and the weaker CH_3 asymmetric vibration (at $\sim 2958 \text{ cm}^{-1}$) as discussed in Matrajt et al. (2005). In six IDPs, the 3.4 μm aliphatic carbon features yield $0.27 \leq \text{C/Si} \leq 1.4$ with a mean $\text{C/Si} = 0.55 \pm 0.43$ (see Table 4 of Matrajt et al. 2005). For three out of the six IDPs, acid dissolution of the silicates allowed the detection of the intrinsically weaker aromatic skeletal ring stretch $\text{C}=\text{C}$ at 6.25 μm (1600 cm^{-1}), which raises the atomic ratios for these three IDPs from $\text{C}_{\text{aliphatic}}/\text{Si} = \{0.78, 0.11, 0.55\}$ to $\text{C}_{\text{aliphatic}+\text{aromatic}}/\text{Si} = \{19.4, 3.1, 5.1\}$ (see Table 5 of Matrajt et al. 2005).

Most IDPs, however, do not possess an aromatic 3.28 μm feature from C-H peripheral bonds on $\text{C}=\text{C}$

skeletal rings. Keller et al. (2004) suggest the lack of the 3.28 μm aromatic feature is due to “much of the carbonaceous matter is comprised very poorly graphitized carbon, possessing only short range order ($< 2 \text{ nm}$), or very large PAH molecules.” The $\text{C}=\text{C}$ bonds that are better tracers of the aromatics than the peripheral C-H bonds. As yet, no comet has been observed with organic features that are of comparable absorbance as the silicate features as observed in absorption spectra of three UCAMMs, where organic absorbances are as strong as for the silicate features (Dartois et al. 2018). As other authors suggest, we infer comets have less “outer disk processed organics” than UCAMMs. This conjecture is also supported by noting the ratio of nitrogen-to-carbon (N/C) in 67P/Churyumov-Gerasimenko is less than the N/C in UCAMMs (Bardyn et al. 2017; Dartois et al. 2018). If IR spectra of cometary comae were to detect the 3.4 μm feature at about the same contrast to the silicate feature as is in laboratory absorbance spectra of IDPs (Matrajt et al. 2005; Brunetto et al. 2014; Merouane et al. 2016), then we may infer that C/Si for our comets that we analyze might increase $\sim 20\%$.

3.9.2. The C/Si gradient in the Solar System

We derived the C/Si atomic ratio using the thermal model dust compositions (and relevant atomic amu) described in §3.3 and the relative masses of the sub-micron grains for each composition returned from the best-fit thermal model. The asymmetric uncertainties in the relative masses derived from the thermal models were ‘symmetrized’ following the description discussed by Audi et al. (Method#2, 2017), cognizant of the limitations to this approach (see Possolo et al. 2019; Barlow 2003) to enable standard error propagation techniques. The carbon to silicon atomic ratio is defined as:

$$\begin{aligned} \frac{C}{Si} &= \frac{C}{\Sigma(Si_{\text{species}}^{\text{dust}})} \\ &= \frac{N_p(C) \cdot C_{\text{amu}}}{\frac{N_p(\text{AO})}{\alpha} + \frac{N_p(\text{AP})}{\beta} + \frac{N_p(\text{CO})}{\delta} + \frac{N_p(\text{CP})}{\gamma}} \end{aligned} \quad (1)$$

where

$$\begin{aligned} \alpha &= \frac{(0.5 \cdot \text{Mg}_{\text{amu}} + 0.5 \cdot \text{Fe}_{\text{amu}}) \times 2 + \text{Si}_{\text{amu}} + 4 \cdot \text{O}_{\text{amu}}}{\text{Si}_{\text{amu}}} \\ \beta &= \frac{(0.5 \cdot \text{Mg}_{\text{amu}} + 0.5 \cdot \text{Fe}_{\text{amu}}) + \text{Si}_{\text{amu}} + 3 \cdot \text{O}_{\text{amu}}}{\text{Si}_{\text{amu}}} \\ \delta &= \frac{(\text{Mg}_{\text{amu}}) \times 2 + \text{Si}_{\text{amu}} + 4 \cdot \text{O}_{\text{amu}}}{\text{Si}_{\text{amu}}} \\ \gamma &= \frac{(\text{Mg}_{\text{amu}}) + \text{Si}_{\text{amu}} + 3 \cdot \text{O}_{\text{amu}}}{\text{Si}_{\text{amu}}} \end{aligned} \quad (2)$$

are the α, β, γ , and δ are the number of Si atoms per unit mass, and the values for N_p (the number of grains

at the peak $[a_p]$ of the HGSD) are found in Table 3. Table 4 summarizes derived the C/Si atomic ratios for comet C/2013 US₁₀ (Catalina) and other comets observed with SOFIA (+FORCAST) as well as comet C/1995 O1 (Hale-Bopp) (Harker et al. 2002). The C/Si atomic ratio for the comets in Table 4, UCAMMs (data from Dartois et al. 2018), and IDPs and other comets (data from Bergin et al. 2015) are presented in Fig. 8. Recent measurements of solar cosmic abundances creates an upper limit for the ISM C/Si of 10 as discussed in Dartois et al. (2018, and references therein). UCAMMs are above the solar cosmic abundance limit. Thus those who study UCAMMs suggest that their organics have sequestered carbon from the gas phase and converted it to a solid phase in the cold outer disk or on the surfaces of nitrogen-rich cold body surfaces because of their enhanced N/C ratios (Dartois et al. 2013, 2018). As measured or computed, cometary comae appear to lack the high C/Si ratios of UCAMMs.

Comets by their C/Si appear to be sampling similar abundances of carbon in the optically active composition of comae particles as SEM-EDX-derived C/Si ratios are measuring for IDPs. Many but not all comets have C/Si commensurate with IDPs, and IDPs are more carbon-rich than carbonaceous chondrites (Fig. 8). Two sun-grazing comets from the Kreutz family of comets, C/2003 K7 and C/2011 W3 (Lovejoy), have silicate-rich dust and fall in the carbonaceous chondrites (CC) range (Bergin et al. 2015; McCauley et al. 2013; Ciaravella et al. 2010).

Gail & Trieloff (2017), Dartois et al. (2018, 2013) and other authors suggest that there was a carbon gradient in the early solar system. The comet C/Si values supports this contention of gradient in the carbon with heliocentric distance of formation. Commensurate with these results, CONSERT on *Rosetta/Philae* suggest comets are a large carbon reservoir given the nucleus' permittivity and density constraints on the dust composition in the nucleus Herique et al. (2016), which agrees within uncertainties with the average specific density of dust particles in the comet C/2013 US₁₀ (Catalina)'s comae. The existence of a carbon gradient in solar systems also is bolstered by the C/Si ratios of IDPs.

Destruction of carbon occurred in inner disk, which is the long-standing “carbon deficit problem” (Bergin et al. 2015; Lee et al. 2010). Disk modelers are working to predict the carbon depletion gradient with complex chemical networks (Wei et al. 2019). Another model investigates removal of carbon through oxidation and photolysis when particles are transported to the exposed upper disk layers but radial transport erases signatures unless other mechanisms quickly destroy carbon like flash heating from FU Ori outbursts or mechanisms prevent replenishment of the inner disk such as sustained particle drift barrier, i.e., a gap opened by the formation of a giant planet. Klarmann et al. (2018) argue that “a

sustained drift barrier or strongly reduced radial grain mobility is necessary to prevent replenishment of carbon from the outer disk [to the inner disk].”

Heat and/or high oxygen fugacity conditions in the inner protoplanetary disk can convert carbon from its incorporation in refractory particles to carbon in gas phase CO or CO₂. As discussed (§3.7.1), particle temperatures above ~823 K can destroy aliphatic carbon. Flash heating of Mg-Fe silicates in the presence of carbon is a possible formation pathway for Type I chondrules (Connolly et al. 1994). If cometary particles can drift interior to the water evaporation front, then cometary materials may deliver carbon to the inner protoplanetary disk. Delivery of carbon to the gas phase of inner disk by comet grains requires inward delivery mechanisms during the early pebble accretion phase of disk evolution when the motions of aggregating materials are dominated by inward pebble drift (Andrews 2020; Misener et al. 2019). Such delivery requires that amorphous carbon particles already be incorporated into cometary grains in addition to the need that the sublimation temperature of amorphous carbon be higher than water ice so that the delivery of carbon particles is interior enough for carbon to become enhanced in the gas phase. High carbon abundances in the gas phase are required to explain the poorly graphitized carbon (PGC) halos around Fe cores in two terminal *Stardust* particles (Wirick et al. 2009; De Gregorio et al. 2017).

Earth's bulk C/Si atomic ratio is much smaller and models for its core formation and evolution assume a carbonaceous chondrite supply of carbon was available to form the Earth (Bergin et al. 2015). Cometary C/Si atomic ratios are much higher than carbonaceous chondrites. The outer disk was richer in carbon than the inner disk. The carbon gradient may be another indication of planetary gaps sculpting the compositions of small bodies. Burkhardt et al. (2019) hypothesize that the isotope variances of planetary bodies, traced through meteoritic and IDPs, can be explained if there were isotopically distinct nebular reservoirs of non-carbonaceous and carbonaceous that were not fully mixed in the primordial disk of the solar system. A planetary gap created by Jupiter's formation which inhibited mixing between the inner and outer disk could also explain the dichotomy in between non-carbonaceous and carbonaceous meteorites (Nanne et al. 2019).

Cometary C/Si atomic ratios highlight the “carbon deficit” that occurred in the inner disk and the dichotomy between the inner and outer disk when juxtaposed with the C/Si atomic ratios found for the Earth and ordinary chondrites. Furthermore, the dust composition of many comets demonstrates a carbon-rich reservoir existed in the regimes of comet formation that are pertinent to the understanding the evolution of our protoplanetary disk and the formation of the planets.

3.10. Dust Production Rates

Table 4. Derived Carbon-to-Silicon Atomic Ratio of Comets^a

Comet	Telescope/Instrument	C/Si	(Ref.)
C/2013 US10 (Catalina)	IRTF (+BASS)	4.180 ± 0.308	(1)
C/2013 US10 (Catalina)	SOFIA (+FORCAST)	6.556 ± 3.262	(1)
C/2013 K1 (Pan-STARRS)	SOFIA (+FORCAST)	3.841 ± 1.086	(2)
C/2013 X1 (Pan-STARRS)	SOFIA (+FORCAST)	7.781 ± 6.091	(3)
C/2018 W2 (Africano)	SOFIA (+FORCAST)	6.204 ± 3.858	(3)
C/1995 O1 (Hale-Bopp)	IRTF (+HIFOGS)	0.420 ± 0.001	(4)

NOTE—References: (1) This work. (2) Woodward et al. (2015). (3) Woodward et al. (2020). (4) Harker et al. (2002).

^aComputed from relative mass ratios of thermal model dust composition components, adopting an amorphous carbon density $\rho = 1.5 \text{ g cm}^{-3}$. Appendix A provides the complete model tables, including revision to C/2013 K1 (Pan-STARRS) and C/1995 O1 (Hale-Bopp) models resulting from an amorphous carbon specific density $\rho_s(\text{ACar}) = 1.5 \text{ g cm}^{-3}$.

The optical spectra of comets in the i' -band tends to be dominated by dust. However, red CN gas emission bands, CN(2,0) and CN(3,1), can present at redder wavelengths within the i' -band (Cochran et al. 2015; Fink et al. 1991; Swings 1956). Presence of these emission lines may contaminate measurements of the scattered light dust continuum surface brightness, and hence estimates of the dust production rate. Optical spectra of comet C/2013 US₁₀ (Catalina) obtained on 2015 December 18 (Kwon et al. 2017) show weak CN(2,0) and CN(3,1) band emission. However, optical spectra obtained after the epoch of the MORIS and FPI+ imagery in 2016 March 18 show no strong emission features redward of 7630 Å to the i' -band long wavelength cut-off (Hyland et al. 2019). The azimuthally-averaged radial profiles of comet C/2013 US₁₀ (Catalina) derived from the MORIS and FPI+ imagery, presented in Fig. 9, shows little deviation from a $1/\rho$ profile (Gehrz & Ney 1992) at large cometo-centric distances consistent with a steady-state coma without significant CN contamination. Application of standard comet image enhancement techniques to these optical data (see Samarasinha & Larson 2014; Samarasinha et al. 2014), reveal no structures in the coma such as jets or spirals at this epoch.

The dust production rate of comet C/2013 US₁₀ (Catalina) during the epoch of the BASS observations (2016 Jan 10.607 UT) was derived using the proxy quantity $Af\rho$ (A'Hearn et al. 1984). When the cometary coma is in steady state, this aperture independent quantity can be parameterized as

In this relation, $A(\theta)$ is four times the *geometric* albedo at a phase angle θ , f is the filling factor of the coma, m_{comet} is the measured cometary magnitude, m_{\odot} is the apparent solar magnitude, derived⁷ as $i'_{\odot} = -27.002$, ρ is the linear radius of the aperture at the comet's position (cm) and r_h (AU) and Δ (cm) are the heliocentric and geocentric distances, respectively.

The Halley-Marcus (HM) (Marcus 2007a,b; Schleicher et al. 1998) phase angle correction⁸ was used to normalize $A(\theta)f\rho$ to 0° phase angle, wherein we adopted an interpolated value of $\text{HM} = 0.3424$ and 0.3946 commensurate with the epoch of our optical observations on 2016 Jan 11.633 UT and 2016 February 09.340 UT, respectively. Table 5 reports values of $A(0^\circ)f\rho = (A(\theta)f\rho/\text{HM})$ at a selection of aperture sizes (distances from the comet photocenter) in the i' -band. The dust production rate is similar to that observed in other moderately active comets, such as C/2012 K1 (Pan-STARRS) discussed by Woodward et al. (2015).

We can roughly estimate the dust mass loss rate by taking the mass of dust observed in the coma inside of our aperture as the $1/\rho$ dependence of the surface brightness distribution indicates a steady state coma. If we adopt for the outflow velocity of 100 μm -radii and larger particles which carry most of the mass a value of $\overline{v}_{\text{dust}} \approx 20 \text{ m s}^{-1}$ (Rinaldi et al. 2018), and assume a steady outflow of material through a spherical bubble at

$$A(\theta)f\rho = \frac{4 r_h^2 \Delta^2 10^{-0.4(m_{\text{comet}} - m_{\odot})}}{\rho} \text{ cm.} \quad (3)$$

⁷ <http://classic.sdss.org/dr5/algorithms/sdssUBVRITransform.html#vega-s>

⁸ <http://asteroid.lowell.edu/comet/dustphase.html>

some distance $R(m)$ near the nucleus surface, the mass loss rate can be estimated as

$$\dot{M}_{\text{dust}} \approx \frac{3 \cdot M_{\text{dust}} \times \overline{v_{\text{dust}}}}{R} \quad (4)$$

where \dot{M}_{dust} has units of g s^{-1} . If the nucleus of comet C/2013 US₁₀ (Catalina) is comparable in size typically inferred for many comets, 1.5 km, then $\dot{M}_{\text{dust}} \approx 4 \times 10^{-3} M_{\text{dust}} [\overline{v_{\text{dust}}}/20(\text{m s}^{-1})]$. At 1.7 au when $M_{\text{dust}} = 4 \times 10^8 \text{ g}$ (Table 3) then $\dot{M}_{\text{dust}} \approx 1.6 \times 10^6 \text{ g s}^{-1}$.

Fink & Rubin (2012) discuss how the $A(\theta)f\rho$ can be tied to the mass production rate, given the HGSD parameters, computing dust mass loss rate (in kg s^{-1}) assuming a particle density of 1 g cm^{-3} for various particle size distribution functions. Taking an average value of $N = 3.5$, corresponding to a $dq/da \sim a^{-3.5}$ which

yielded a mass loss rate of 22.8 k s^{-1} from the detailed computations of Fink & Rubin (2012, see Table 2) and using a A_f at zero phase for C/2013 US₁₀ (Catalina) of $\sim 6290 \text{ cm}$ (Table 5) one finds $\dot{M}_{\text{dust}} \approx 2.4 \times 10^6 \text{ g s}^{-1}$. This is comparable our latter estimate.

If we assume the density of the nucleus, which is a porous dust-ice mixture, is $\rho_{\text{nuc}} \sim 1 \text{ g cm}^{-3}$ (Fulle et al. 2019) then a rough estimate of the surface erosion rate

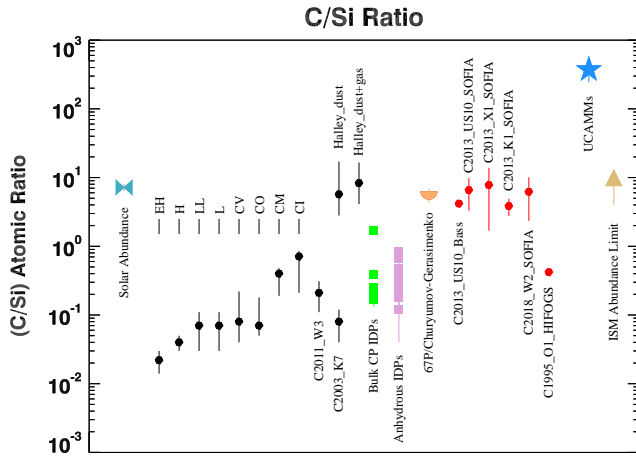


Figure 8. Atomic carbon-to-silicon ratio for various small bodies relevant to comets. Ratios from (Bergin et al. 2015, supplemental appendix) are given with black filled circles, while those derived for comets from our thermal model analysis (see §3.9.2) are indicated with the red filled circles. Also depicted by the filled green squares are five values for chondritic porous (CP) interplanetary dust particles (IDPs) from Keller et al. (2004), the purple filled squares are values for 19 anhydrous IDPs measured by Thomas et al. (1993b), and the half-filled circle is average value of the C/S atomic ratio of comet 67P/Churyumov-Gerasimenko particles studied by Bardin et al. (2017). The blue star denotes the values for the UltraCarbonaceous Antarctic MicroMeteorites (UCAMMs) while the limit to the interstellar medium C/Si atomic ratio, brown triangle, is from Dartois et al. (2018). Both C/2011 W3 and C/2003 K7 are sun grazing comets and the determination of the C/Si atomic ratio in these objects is derived from ultra-violet measurements when these comets were in the solar corona (see Bergin et al. 2015, and references therein). The solar abundance values are taken from Lodders (2010) and references therein.

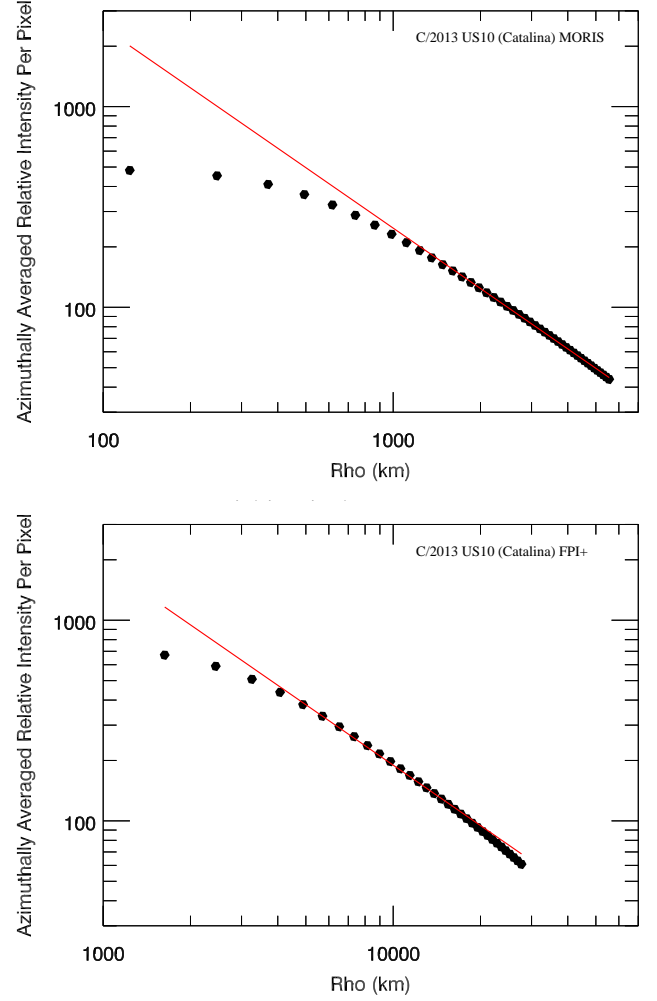


Figure 9. Azimuthally averaged relative intensity per pixel as a function of linear radius (ρ) in km as measured in a SDSS i' -band filter from the optical photocenter (centroid) of comet C/2013 US₁₀ (Catalina). The solid red line denotes a $1/\rho$ profile describing a steady-state coma (see Gehrz & Ney 1992). Top: the IRTF MORIS data obtained on 2016 Jan 11.63 UT when the phase angle was 47.80 degrees. Bottom: the SOFIA FPI+ data obtained on 2016 Feb 09.34 UT when the phase angle was 33.06 degrees. Note the change in scale between the two epochs.

from the nucleus of comet C/2013 US₁₀ (Catalina) is $\sim 1 \text{ mm day}^{-1}$ if the entire surface is active and if the radius of the comet is $\sim 1.5 \text{ km}$. The depth of space weathering of an DN comet in the local interstellar medium might be at most a centimeter over the age of the solar system and this material would be shed in a timeframe of $\lesssim 2$ weeks at the observed dust mass loss rate which we have translated to an erosion rate. For a perspective, cumulative erosion depths for comet 67P/Churyumov-Gerasimenko depended on the nucleus geography and solar insolation and from start of the *Rosetta* mission until the first equinox were 6 mm to 0.1 m and to the end of the mission were of order 0.3 m to 4 m (Combi et al. 2020).

The quantity $\epsilon f \rho$, (see Appendix A of Kelley et al. 2013), a parameter which is the thermal emission corollary of the scattered-light based light $A f \rho$ was also computed using our FORCAST broadband photometry. $\epsilon f \rho$ is defined as

$$\epsilon f \rho = \frac{\Delta^2 F_\nu}{\pi \rho B_\nu} (\text{cm}), \quad (5)$$

where ϵ is the effective dust emissivity, F_ν is the flux density (Jy) of the comet within the aperture of radius ρ , B_ν is the Planck function (Jy/sr) evaluated at the temperature $T_c = T_{\text{bb}} = 1.093 \times (278 \text{ K}) r_h^{-0.5} \simeq 232.9 \text{ K}$, where T_c is the color temperature. Derived values of $\epsilon f \rho$ for comet C/2013 US₁₀ (Catalina) from SOFIA photometry are presented in Table 2.

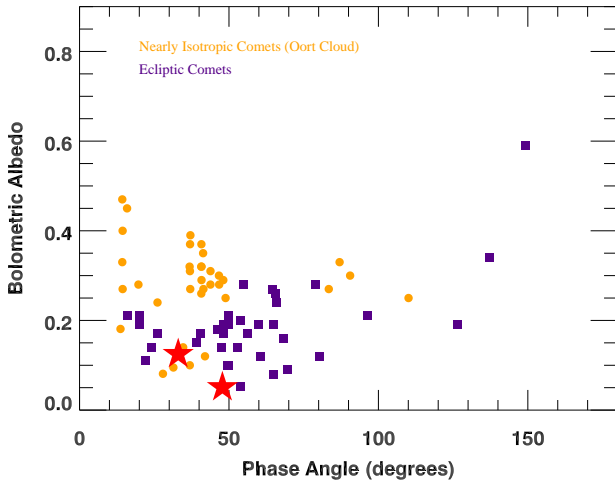


Figure 10. The bolometric albedo of ecliptic and nearly isotropic comets (Oort cloud comets) as a function of phase angle. Estimates for comet C/2013 US₁₀ (Catalina) are depicted by the filled red stars for both the NASA IRTF ($\simeq 5\%$, 2016 Jan 10 UT) and NASA SOFIA ($\simeq 14\%$, 2016 Feb 09 UT) observations. The bolometric albedo of C/2013 US₁₀ (Catalina) is low compared to other isotropic (Oort cloud) comets.

3.11. Dust Bolometric Albedo

Our near simultaneous optical observations conducted on the same night as our measurement of the infrared SED of comet C/2013 US₁₀ (Catalina) enable us to estimate the *bolometric* dust albedo as described by Woodward et al. (2015). The measured albedo depends on both the composition and structure of the dust grains as well as the phase angle (Sun-comet observer angle) of the observations. As the grain albedo is the ratio of the scattered light to the total incident radiation, the thermal emission at IR wavelengths and the scattered light component observed at optical wavelengths are linked though this parameter.

The photometry from the *i'* imagery in an equivalent aperture that corresponds to the apertures used to measure the IR SEDs provides an estimate of $[\lambda F_\lambda]_{\text{scattering}}^{\text{max}}$. An estimate of $[\lambda F_\lambda]_{\text{IR}}^{\text{max}}$ is obtained from a filter integrated equivalent photometric point at $10 \mu\text{m}$ derived by integrating with the observed IR SED over the bandwidth of the FORCAST F111 filter. We find that the coma of comet Oort cloud C/2013 US₁₀ (Catalina) has a low bolometric dust albedo, $A(\theta)$, of $\simeq 5.1 \pm 0.1\%$ at phase angle of 47.80° and to $\simeq 13.8 \pm 0.5\%$ at a phase angle of 33.01° .

Fig. 10 shows the derived $A(\theta)$ as a function of phase angle, θ for a variety of comets, where the red stars denoted the values for C/2013 US₁₀ (Catalina). At 1.3 AU, the bolometric albedo of comet C/2013 US₁₀ (Catalina) is likely measuring the reflectance properties of the refractory particles because ice grains have very short lifetimes at this heliocentric distance (Beer et al. 2006; Protopapa et al. 2018). Reflectance of individual refractory particles from the coma of comet 67P/Churyumov-Gerasimenko as measured by *Rosetta* COSIMA/Cosicope are from 3% to 22% at 650 nm (Langevin et al. 2017, 2020), which spans the range of bolometric albedos measured for comet comae.

4. CONCLUSION

Mid-infrared $6.0 \lesssim \lambda(\mu\text{m}) \lesssim 40$ spectrophotometric observations of comet C/2013 US₁₀ (Catalina) at two temporal epochs yielded an inventory of the refractory materials in the comet's coma and their physical characteristics through thermal modeling analysis. The coma of C/2013 US₁₀ (Catalina) has a high abundance of submicron-radii moderately porous (fractal porosity $D = 2.727$) carbonaceous amorphous grains with a silicate-to-carbon mass ratio $\lesssim 0.9$. This comet also exhibited a weak $10 \mu\text{m}$ silicate feature.

Comet C/2013 US₁₀ (Catalina) is an example of subset of comets with weak silicate features that are definitively shown to have low silicate-to-carbon ratios for the submicron grain component (as deduced from thermal model analysis of the spectral energy distributions), that is, they are carbon-rich. Their thermal emission is dominated by warmer particles that are significantly more absorbing at UV-near-IR wavelengths than silicates. The

Table 5. $A(0^\circ)f\rho$ Values Comet C/2013 US10 (Catalina)

Aperture	ρ	SDSS $[i]'$	$A(0^\circ)f\rho$
Radius	Radius		
(arcsec)	(km)	(mag)	(cm)
1.82	990.85	13.040 ± 0.003	4618.84 ± 14.72
3.88	1052.78	11.970 ± 0.001	5823.43 ± 0.12
4.56	1238.56	11.771 ± 0.001	5950.71 ± 1.98
9.12	2477.12	10.968 ± 0.002	6230.16 ± 9.93
13.68	7431.36	10.517 ± 0.002	6290.99 ± 10.96
18.24	9908.48	10.235 ± 0.003	6121.96 ± 16.48

NOTE— $Af\rho$ values (computed from SDSS i' filter photometry) corrected to zero phase derived from IRTF (+MORIS) observations on 2016 Jan 11.63 UT.

spectral grasp of SOFIA (+FORCAST) provided a constraint that required the presence of amorphous carbon as a dominate constituent of the coma particle population (submicron dust) as silicate particles cannot provide the lack of contrast above blackbody emission at far-infrared wavelengths. The surface area of the thermal emission is dominated by the smaller grains and for the silicates, the smaller grains produce resonances 19.5, 23.5, 27.5 μm not evident in the spectrum of comet C/2013 US₁₀ (Catalina), which is a puzzle.

A dark refractory carbonaceous material darkens and reddens the surface of the nucleus of 67P/Churyumov-Gerasimenko. Comet C/2013 US₁₀ (Catalina) is carbon-rich. Analysis of comet C/2013 US₁₀ (Catalina) grain composition and observed infrared spectral features compared to interplanetary dust particles, chondritic materials, and *Stardust* samples suggest that the dark carbonaceous material is well-represented by the optical properties of amorphous carbon. We argue that this dark material is endemic to comets.

The C/Si atomic ratio of comets in context with that derived from studies of interplanetary dust particles, micrometeorites, and *Stardust* samples suggest that a carbon gradient was present in the early solar nebula. As we observe more comets, and especially take the opportunities to observe dynamically new comets with SOFIA, the James Webb Space Telescope and other capabilities, a significant subset of comets which are

carbon-rich likely will arise providing important constraints on newly proposed interpretations of disk processing in the primitive solar system.

ACKNOWLEDGMENTS

Based in part on observations made with the NASA/DLR Stratospheric Observatory for Infrared Astronomy (SOFIA). SOFIA is jointly operated by the Universities Space Research Association, Inc. (USRA), under NASA contract NNA17BF53C, and the Deutsches SOFIA Institut (DSI) under DLR contract 50 OK 0901 to the University of Stuttgart. Financial support for this work was provided by NASA through award SOF 04-0010 and NASA PAST grant 80NSSC19K0868. The authors wish to thank Dr. Aigen Lee for informative discussion regarding carbonaceous materials and there relevance to interpreting astronomical spectra as well as Dr. Jeff Cuzzi and the NASA Ames research group for their keen insights into disk transport models. The authors also express gratitude for the two anonymous referees' very careful reading of the manuscript and their numerous suggestions and comments that enhanced the final narrative.

Facilities: NASA SOFIA (FORCAST/FPI+), NASA IRTF (BASS/MORIS)

Software: IRAF (Tody 1986, 1993), IDL, JPL Horizons (Giorgini et al. 1996), Aperture Photometry Tool (APT) Laher et al. (2012)

APPENDIX

A. TABLES OF REVISED THERMAL MODELS

As described in the text (§3.2.6) we have adopted a value for 1.5 g cm⁻³ for the specific density of amorphous carbon, $\rho_s(\text{ACar})$, in our thermal models. In early work, we employed a higher specific density of 2.5 g cm⁻³. In order

Table 6. Derived Grain Composition of Comet C/2012 K1 (Pan-STARRS)^a

<u>SOFIA (+FORCAST)^b</u>		
		Relative
		Mass
		Sub- μm
Thermal Model SED Details	$(N_p \times 10^{20})^c$	Grains
<u>Dust Components</u>		
Amorphous pyroxene	$0.658^{+0.084}_{-0.133}$	$0.398^{+0.077}_{-0.085} \times 10^7$
Amorphous olivine	$0.000^{+0.085}_{-0.000}$	$0.000^{+0.054}_{-0.000}$
Amorphous carbon	$1.656^{+0.056}_{-0.057}$	$0.455^{+0.064}_{-0.050}$
Crystalline olivine	$0.181^{+0.161}_{-0.165}$	$0.147^{+0.104}_{-0.133}$
Crystalline pyroxene	0.000	0.000
<u>Resultants</u>		
Total mass sub- μm grains (gm) $\times 10^8$	$3.727^{+0.426}_{-0.449}$...
Amorphous silicate dust fraction	$0.398^{+0.080}_{-0.071}$...
Crystalline silicate dust fraction	$0.147^{+0.104}_{-0.133}$...
Silicate to Carbon ratio [†]	$1.198^{+0.271}_{-0.269}$...
Crystalline silicate mass to total silicate mass ^d	$0.270^{+0.160}_{-0.241}$...
$a_p(\mu\text{m})^e$	0.7	...
Fractal porosity (D)	2.857	...
<u>Other Parameters</u>		
Hanner Grain-Size Distribution M : N	22.2 : 3.7	...
Reduced χ^2_ν	1.06	...
Degrees of freedom	146	...

NOTE—

^aUncertainties represent the 95% confidence level.^bComet on 2014 Jun 06 UT $r_h = 1.70$ au, $\Delta = 1.71$ au.^cNumber of grains, N_p , at the peak (a_p) of the Hanner grain size distribution (GSD).^d $f_{cryst} \equiv m_{cryst}/[m_{amorphous} + m_{cryst}]$ where m_{cryst} is the mass fraction of submicron crystals.^ePeak grain size (radius) of the Hanner GSD.[†]Ratio represents the bulk mass properties of the materials in the models.

to compare the atomic carbon-to-silicate ratios consistently thermal models for all SOFIA observed comets included in this analysis were modeled or remodeled with a common value of $\rho_s(\text{ACar}) = 1.5 \text{ g cm}^{-3}$. Tables for comets C/2012 K1 (Pan-Starrs) (see [Woodward et al. 2015](#)), C/1995 O1 (Hale-Bopp) (see [Harker et al. 2002](#)), and C/2013 X1 (Pan-STARRS) and C/2018 W2 (Africano) ([Woodward et al. 2020](#)) are given for completeness.

Table 7. Derived Grain Composition of Comet C/2013 X1 (Pan-STARRS)^a

<u>SOFIA (+FORCAST)</u> ^b		
Thermal Model SED Details	$(N_p \times 10^{20})$ ^c	Relative
		Mass
		Sub- μm
		Grains
<u>Dust Components</u>		
Amorphous pyroxene	$0.000^{+0.303}_{-0.000}$	$0.000^{+0.268}_{-0.000}$
Amorphous olivine	$0.213^{+0.071}_{-0.191}$	$0.214^{+0.119}_{-0.195}$
Amorphous carbon	$1.197^{+0.064}_{-0.066}$	$0.545^{+0.168}_{-0.149}$
Crystalline olivine	$0.138^{+0.212}_{-0.138}$	$0.241^{+0.213}_{-0.241}$
Crystalline pyroxene	$0.643^{+0.004}_{-0.004}$	$0.046^{+0.001}_{-0.001}$
<u>Resultants</u>		
Total mass sub- μm grains (gm) $\times 10^8$	$1.567^{+0.588}_{-0.353}$...
Amorphous silicate dust fraction	$0.214^{+0.163}_{-0.099}$...
Crystalline silicate dust fraction	$0.241^{+0.213}_{-0.241}$...
Silicate to Carbon ratio [†]	$0.834^{+0.689}_{-0.433}$...
Crystalline silicate mass to total silicate mass ^d	$0.530^{+0.260}_{-0.530}$...
$a_p(\mu\text{m})$ ^e	0.6	...
Fractal porosity (D)	2.727	...
<u>Other Parameters</u>		
Hanner Grain-Size Distribution M : N	18.5 : 3.7	...
Reduced χ^2_ν	0.5806	...
Degrees of freedom	147	...

NOTE—

^aUncertainties represent the 95% confidence level.^bComet on 2016 Jul 13 UT $r_h = 1.80$ au, $\Delta = 1.02$ au.^cNumber of grains, N_p , at the peak (a_p) of the Hanner grain size distribution (GSD).^d $f_{cryst} \equiv m_{cryst}/[m_{amorphous} + m_{cryst}]$ where m_{cryst} is the mass fraction of sub-micron crystals.^ePeak grain size (radius) of the Hanner GSD.[†]Ratio represents the bulk mass properties of the materials in the models.

Table 8. Derived Grain Composition of Comet C/2018 W2 (Africano)^a

<u>SOFIA (+FORCAST)</u> ^b		Relative Mass Sub- μm Grains
Thermal Model SED Details	$(N_p \times 10^{19})$ ^c	
<u>Dust Components</u>		
Amorphous pyroxene	$0.166^{+0.692}_{-0.166}$	$2.698^{+7.153}_{-2.534} \times 10^7$
Amorphous olivine	$0.488^{+0.294}_{-0.488}$	$0.077^{+0.276}_{-0.077}$
Amorphous carbon	$0.308^{+0.300}_{-0.270}$	$0.226^{+0.133}_{-0.225}$
Crystalline olivine	$0.082^{+0.340}_{-0.082}$	$0.647^{+0.166}_{-0.146}$
Crystalline pyroxene	0.000	0.000
<u>Resultants</u>		
Total mass sub- μm grains (gm) $\times 10^{18}$	$0.000^{+3.719}_{-0.000}$...
Amorphous silicate dust fraction	$0.050^{+0.166}_{-0.050}$...
Crystalline silicate dust fraction	$0.000^{+0.187}_{-0.000}$...
Silicate to Carbon ratio [†]	$0.303^{+0.122}_{-0.161}$...
Crystalline silicate mass to total silicate mass ^d	$0.050^{+0.224}_{-0.050}$...
$a_p(\mu\text{m})$ ^e	0.4	...
Fractal porosity (D)	2.857	...
<u>Other Parameters</u>		
Hanner Grain-Size Distribution M : N	10.2 : 3.4	...
Reduced χ^2	0.84	...
Degrees of freedom	134	...

NOTE—

^aUncertainties represent the 95% confidence level.^bComet on 2019 Oct 18 UT $r_h = 1.60$ au, $\Delta = 0.84$ au.^cNumber of grains, N_p , at the peak (a_p) of the Hanner grain size distribution (GSD).^d $f_{cryst} \equiv m_{cryst}/[m_{amorphous} + m_{cryst}]$ where m_{cryst} is the mass fraction of submicron crystals.^ePeak grain size (radius) of the Hanner GSD.[†]Ratio represents the bulk mass properties of the materials in the models.

Table 9. Derived Grain Composition of Comet C/1995 O1 (Hale-Bopp)^a

<u>HIFOGS + ISO Spectra</u> ^b		Relative
		Mass
		Sub- μm
Thermal Model SED Details	$(N_p \times 10^{22})$ ^c	Grains
<u>Dust Components</u>		
Amorphous pyroxene	$5.552^{+0.009}_{-0.009}$	$0.304^{+0.001}_{-0.001}$
Amorphous olivine	$6.334^{+0.005}_{-0.005}$	$0.347^{+0.001}_{-0.001}$
Amorphous carbon	$3.169^{+0.002}_{-0.002}$	$0.079^{+0.001}_{-0.001}$
Crystalline olivine	$3.182^{+0.002}_{-0.002}$	$0.224^{+0.001}_{-0.001}$
Crystalline pyroxene	$0.643^{+0.004}_{-0.004}$	$0.046^{+0.001}_{-0.001}$
<u>Resultants</u>		
Total mass sub- μm grains (gm) $\times 10^8$	$420.133^{+0.009}_{-0.006}$...
Amorphous silicate dust fraction	$0.651^{+0.001}_{-0.001}$...
Crystalline silicate dust fraction	$0.270^{+0.001}_{-0.001}$...
Silicate to Carbon ratio [†]	$11.678^{+0.008}_{-0.008}$...
Crystalline silicate mass to total silicate mass ^d	$0.293^{+0.001}_{-0.001}$...
$a_p(\mu\text{m})$ ^e	0.2	...
Fractal porosity (D)	2.857	...
<u>Other Parameters</u>		
Hanner Grain-Size Distribution M : N	3.4 : 3.4	...
Reduced χ^2_ν	11015.16	...
Degrees of freedom	513	...

NOTE—

^aUncertainties represent the 95% confidence level.^bComet on 1995 Oct 11 UT $r_h = 2.80$ au, $\Delta = 3.03$ au.^cNumber of grains, N_p , at the peak (a_p) of the Hanner grain size distribution (GSD).^d $f_{cryst} \equiv m_{cryst}/[m_{amorphous} + m_{cryst}]$ where m_{cryst} is the mass fraction of sub-micron crystals.^ePeak grain size (radius) of the Hanner GSD.[†]Ratio represents the bulk mass properties of the materials in the models.

REFERENCES

- Ábrahám, P., Chen, L., Kóspál, Á., et al. 2019, *ApJ*, 887, 156, doi: [10.3847/1538-4357/ab521d](https://doi.org/10.3847/1538-4357/ab521d)
- A’Hearn, M. F., Schleicher, D. G., Millis, R. L., Feldman, P. D., & Thompson, D. T. 1984, *AJ*, 89, 579, doi: [10.1086/113552](https://doi.org/10.1086/113552)
- A’Hearn, M. F., Belton, M. J. S., Delamere, W. A., et al. 2005, *Science*, 310, 258, doi: [10.1126/science.1118923](https://doi.org/10.1126/science.1118923)
- Alexander, C. M. O. D., Cody, G. D., De Gregorio, B. T., Nittler, L. R., & Stroud, R. M. 2017, *Chemie der Erde / Geochemistry*, 77, 227, doi: [10.1016/j.chemer.2017.01.007](https://doi.org/10.1016/j.chemer.2017.01.007)
- Alexander, C. M. O. D., Fogel, M., Yabuta, H., & Cody, G. D. 2007, *GeoCoA*, 71, 4380, doi: [10.1016/j.gca.2007.06.052](https://doi.org/10.1016/j.gca.2007.06.052)
- Andrews, S. M. 2020, arXiv e-prints, arXiv:2001.05007. <https://arxiv.org/abs/2001.05007>
- Audi, G., Kondev, F. G., Wang, M., Huang, W. J., & Naimi, S. 2017, *Chinese Physics C*, 41, 030001, doi: [10.1088/1674-1137/41/3/030001](https://doi.org/10.1088/1674-1137/41/3/030001)
- Bai, X.-N. 2016, *ApJ*, 821, 80, doi: [10.3847/0004-637X/821/2/80](https://doi.org/10.3847/0004-637X/821/2/80)
- Baratta, G. A., Mennella, V., Brucato, J. R., et al. 2004, *Journal of Raman Spectroscopy*, 35, 487, doi: [10.1002/jrs.1169](https://doi.org/10.1002/jrs.1169)
- Bardyn, A., Baklouti, D., Cottin, H., et al. 2017, *MNRAS*, 469, S712, doi: [10.1093/mnras/stx2640](https://doi.org/10.1093/mnras/stx2640)
- Barlow, R. 2003, in *Statistical Problems in Particle Physics, Astrophysics, and Cosmology*, ed. L. Lyons, R. Mount, & R. Reitmeyer, 250. <https://arxiv.org/abs/physics/0401042>
- Beer, E. H., Podolak, M., & Prialnik, D. 2006, *Icarus*, 180, 473, doi: [10.1016/j.icarus.2005.10.018](https://doi.org/10.1016/j.icarus.2005.10.018)
- Belton, M. J. S., Thomas, P., Veverka, J., et al. 2007, *Icarus*, 187, 332, doi: [10.1016/j.icarus.2006.09.005](https://doi.org/10.1016/j.icarus.2006.09.005)
- Bergin, E. A., Blake, G. A., Ciesla, F., Hirschmann, M. M., & Li, J. 2015, *Proceedings of the National Academy of Science*, 112, 8965, doi: [10.1073/pnas.1500954112](https://doi.org/10.1073/pnas.1500954112)
- Bockelée-Morvan, D., Brooke, T. Y., & Crovisier, J. 1995, *Icarus*, 116, 18, doi: [10.1006/icar.1995.1111](https://doi.org/10.1006/icar.1995.1111)
- Bockelée-Morvan, D., Rinaldi, G., Erard, S., et al. 2017a, *MNRAS*, 469, S443, doi: [10.1093/mnras/stx1950](https://doi.org/10.1093/mnras/stx1950)
- . 2017b, *MNRAS*, 469, S842, doi: [10.1093/mnras/sty533](https://doi.org/10.1093/mnras/sty533)
- Bockelée-Morvan, D., Leyrat, C., Erard, S., et al. 2019, *A&A*, 630, A22, doi: [10.1051/0004-6361/201834764](https://doi.org/10.1051/0004-6361/201834764)
- Bohren, C. F., & Huffman, D. R. 1983, *Absorption and scattering of light by small particles*
- Bradley, J. P. 2013, *GeoCoA*, 107, 336, doi: [10.1016/j.gca.2012.04.061](https://doi.org/10.1016/j.gca.2012.04.061)
- Bradley, J. P., Keller, L. P., Snow, T. P., et al. 1999, *Science*, 285, 1716, doi: [10.1126/science.285.5434.1716](https://doi.org/10.1126/science.285.5434.1716)
- Brownlee, D. 2014, *Annual Review of Earth and Planetary Sciences*, 42, 179, doi: [10.1146/annurev-earth-050212-124203](https://doi.org/10.1146/annurev-earth-050212-124203)
- Brownlee, D., Tsou, P., Aléon, J., et al. 2006, *Science*, 314, 1711, doi: [10.1126/science.1135840](https://doi.org/10.1126/science.1135840)
- Brownlee, D. E., & Joswiak, D. J. 2017, *Meteoritics and Planetary Science*, 52, 471, doi: [10.1111/maps.12804](https://doi.org/10.1111/maps.12804)
- Brunetto, R., Borg, J., Dartois, E., et al. 2011, *Icarus*, 212, 896, doi: [10.1016/j.icarus.2011.01.038](https://doi.org/10.1016/j.icarus.2011.01.038)
- Brunetto, R., Lantz, C., Ledu, D., et al. 2014, *Icarus*, 237, 278, doi: [10.1016/j.icarus.2014.04.047](https://doi.org/10.1016/j.icarus.2014.04.047)
- Burkhardt, C., Dauphas, N., Hans, U., Bourdon, B., & Kleine, T. 2019, *GeoCoA*, 261, 145, doi: [10.1016/j.gca.2019.07.003](https://doi.org/10.1016/j.gca.2019.07.003)
- Busemann, H., Nguyen, A. N., Cody, G. D., et al. 2009, *Earth and Planetary Science Letters*, 288, 44, doi: [10.1016/j.epsl.2009.09.007](https://doi.org/10.1016/j.epsl.2009.09.007)
- Ciaravella, A., Raymond, J. C., & Giordano, S. 2010, *ApJL*, 713, L69, doi: [10.1088/2041-8205/713/1/L69](https://doi.org/10.1088/2041-8205/713/1/L69)
- Ciesla, F. J. 2011, *ApJ*, 740, 9, doi: [10.1088/0004-637X/740/1/9](https://doi.org/10.1088/0004-637X/740/1/9)
- Ciesla, F. J., & Sandford, S. A. 2012, *Science*, 336, 452, doi: [10.1126/science.1217291](https://doi.org/10.1126/science.1217291)
- Clarke, M., Vacca, W. D., & Shuping, R. Y. 2015, *Astronomical Society of the Pacific Conference Series*, Vol. 495, *Redux: A Common Interface for SOFIA Data Reduction Pipelines*, ed. A. R. Taylor & E. Rosolowsky, 355
- Clemett, S. J., Sandford, S. A., Nakamura-Messenger, K., Hörz, F., & McKay, D. S. 2010, *Meteoritics and Planetary Science*, 45, 701, doi: [10.1111/j.1945-5100.2010.01062.x](https://doi.org/10.1111/j.1945-5100.2010.01062.x)
- Cochran, A. L., Lvasseur-Regourd, A.-C., Cordiner, M., et al. 2015, *SSRv*, 197, 9, doi: [10.1007/s11214-015-0183-6](https://doi.org/10.1007/s11214-015-0183-6)
- Combi, M., Shou, Y., Fougere, N., et al. 2020, *Icarus*, 335, 113421, doi: [10.1016/j.icarus.2019.113421](https://doi.org/10.1016/j.icarus.2019.113421)
- Connolly, H. C., Hewins, R. H., Ash, R. D., et al. 1994, *Nature*, 371, 136, doi: [10.1038/371136a0](https://doi.org/10.1038/371136a0)
- Cottin, H., & Fray, N. 2008, *SSRv*, 138, 179, doi: [10.1007/s11214-008-9399-z](https://doi.org/10.1007/s11214-008-9399-z)
- Crovisier, J., & Bockelée-Morvan, D. 2008, *Icarus*, 195, 938, doi: [10.1016/j.icarus.2007.08.045](https://doi.org/10.1016/j.icarus.2007.08.045)
- Crovisier, J., Leech, K., Bockelée-Morvan, D., et al. 1997, *Science*, 275, 1904, doi: [10.1126/science.275.5308.1904](https://doi.org/10.1126/science.275.5308.1904)
- Crovisier, J., Brooke, T. Y., Hanner, M. S., et al. 1996, *A&A*, 315, L385
- Cuzzi, J. N., Hogan, R. C., Paque, J. M., & Dobrovolskis, A. R. 2001, *ApJ*, 546, 496, doi: [10.1086/318233](https://doi.org/10.1086/318233)

- Dartois, E., Engrand, C., Duprat, J., et al. 2018, *A&A*, 609, A65, doi: [10.1051/0004-6361/201731322](https://doi.org/10.1051/0004-6361/201731322)
- Dartois, E., Engrand, C., Brunetto, R., et al. 2013, *Icarus*, 224, 243, doi: [10.1016/j.icarus.2013.03.002](https://doi.org/10.1016/j.icarus.2013.03.002)
- de Bergh, C., Schmitt, B., Moroz, L. V., Quirico, E., & Cruikshank, D. P. 2008, *Laboratory Data on Ices, Refractory Carbonaceous Materials, and Minerals Relevant to Transneptunian Objects and Centaurs*, ed. M. A. Barucci, H. Boehnhardt, D. P. Cruikshank, A. Morbidelli, & R. Dotson, 483
- De Gregorio, B. T., Stroud, R. M., Nittler, L. R., & Kilcoyne, A. L. D. 2017, *ApJ*, 848, 113, doi: [10.3847/1538-4357/aa8c07](https://doi.org/10.3847/1538-4357/aa8c07)
- Defouilloy, C., Joswiak, D. J., Brownlee, D. E., & Kita, N. T. 2018, in *Lunar and Planetary Science Conference, Lunar and Planetary Science Conference*, 2167
- Defouilloy, C., Nakashima, D., Joswiak, D. J., et al. 2016, in *Lunar and Planetary Science Conference, Lunar and Planetary Science Conference*, 1584
- Defouilloy, C., Nakashima, D., Joswiak, D. J., et al. 2017, *Earth and Planetary Science Letters*, 465, 145, doi: [10.1016/j.epsl.2017.02.045](https://doi.org/10.1016/j.epsl.2017.02.045)
- Della Corte, V., Rotundi, A., Zakharov, V., et al. 2019, *A&A*, 630, A25, doi: [10.1051/0004-6361/201834912](https://doi.org/10.1051/0004-6361/201834912)
- Dello Russo, N., Kawakita, H., Vervack, R. J., & Weaver, H. A. 2016, *Icarus*, 278, 301, doi: [10.1016/j.icarus.2016.05.039](https://doi.org/10.1016/j.icarus.2016.05.039)
- Dello Russo, N., Mumma, M. J., DiSanti, M. A., et al. 2006, *Icarus*, 184, 255, doi: [10.1016/j.icarus.2006.04.020](https://doi.org/10.1016/j.icarus.2006.04.020)
- Disanti, M. A., Mumma, M. J., Dello Russo, N., et al. 1999, *Nature*, 399, 662, doi: [10.1038/21378](https://doi.org/10.1038/21378)
- Do-Duy, T., Wright, C. M., Fujiyoshi, T., et al. 2020, *MNRAS*, 493, 4463, doi: [10.1093/mnras/staa396](https://doi.org/10.1093/mnras/staa396)
- Dobrica, E., Engrand, C., Duprat, J., et al. 2009, *Meteoritics and Planetary Science*, 44, 1643, doi: [10.1111/j.1945-5100.2009.tb01196.x](https://doi.org/10.1111/j.1945-5100.2009.tb01196.x)
- Dobrică, E., Engrand, C., Leroux, H., Rouzaud, J. N., & Duprat, J. 2012, *GeoCoA*, 76, 68, doi: [10.1016/j.gca.2011.10.025](https://doi.org/10.1016/j.gca.2011.10.025)
- Dorschner, J., Begemann, B., Henning, T., Jaeger, C., & Mutschke, H. 1995, *A&A*, 300, 503
- Duprat, J., Dobrică, E., Engrand, C., et al. 2010, *Science*, 328, 742, doi: [10.1126/science.1184832](https://doi.org/10.1126/science.1184832)
- Edoh, O. 1983, Ph.D Thesis, University of Arizona, Tucson, AZ
- Estrada, P. R., & Cuzzi, J. N. 2016, in *Lunar and Planetary Science Conference, Lunar and Planetary Science Conference*, 2854
- Estrada, P. R., Cuzzi, J. N., & Morgan, D. A. 2016, *ApJ*, 818, 200, doi: [10.3847/0004-637X/818/2/200](https://doi.org/10.3847/0004-637X/818/2/200)
- Fabian, D., Henning, T., Jäger, C., et al. 2001, *A&A*, 378, 228, doi: [10.1051/0004-6361:20011196](https://doi.org/10.1051/0004-6361:20011196)
- Fink, U., Combi, M. R., & Disanti, M. A. 1991, *ApJ*, 383, 356, doi: [10.1086/170794](https://doi.org/10.1086/170794)
- Fink, U., & Rubin, M. 2012, *Icarus*, 221, 721, doi: [10.1016/j.icarus.2012.09.001](https://doi.org/10.1016/j.icarus.2012.09.001)
- Floss, C., Stadermann, F. J., Bradley, J. P., et al. 2006, *Geochimica et Cosmochimica Acta*, 70, 2371, doi: <https://doi.org/10.1016/j.gca.2006.01.023>
- Flynn, G., Wirick, S., & Keller, L. 2015, in *EGU General Assembly Conference Abstracts, EGU General Assembly Conference Abstracts*, 2977
- Flynn, G. J. 2008, *Earth Moon and Planets*, 102, 447, doi: [10.1007/s11038-007-9214-y](https://doi.org/10.1007/s11038-007-9214-y)
- Flynn, G. J., Keller, L. P., Jacobsen, C., & Wirick, S. 2004, *Advances in Space Research*, 33, 57, doi: [10.1016/j.asr.2003.09.036](https://doi.org/10.1016/j.asr.2003.09.036)
- Flynn, G. J., Wirick, S., & Keller, L. P. 2013, *Earth, Planets, and Space*, 65, 1159, doi: [10.5047/eps.2013.05.007](https://doi.org/10.5047/eps.2013.05.007)
- Frank, D. R., Zolensky, M. E., & Le, L. 2014, *GeoCoA*, 142, 240, doi: [10.1016/j.gca.2014.05.037](https://doi.org/10.1016/j.gca.2014.05.037)
- Fulle, M., Blum, J., Green, S. F., et al. 2019, *MNRAS*, 482, 3326, doi: [10.1093/mnras/sty2926](https://doi.org/10.1093/mnras/sty2926)
- Gail, H. P. 2002, *A&A*, 390, 253, doi: [10.1051/0004-6361:20020614](https://doi.org/10.1051/0004-6361:20020614)
- . 2004, *A&A*, 413, 571, doi: [10.1051/0004-6361:20031554](https://doi.org/10.1051/0004-6361:20031554)
- Gail, H.-P., & Tieloff, M. 2017, *A&A*, 606, A16, doi: [10.1051/0004-6361/201730480](https://doi.org/10.1051/0004-6361/201730480)
- Gainsforth, Z., Butterworth, A. L., Stodolna, J., et al. 2015, *Meteoritics and Planetary Science*, 50, 976, doi: [10.1111/maps.12445](https://doi.org/10.1111/maps.12445)
- Gehrz, R. D., & Ney, E. P. 1992, *Icarus*, 100, 162, doi: [10.1016/0019-1035\(92\)90027-5](https://doi.org/10.1016/0019-1035(92)90027-5)
- Giacalone, S., Teitler, S., Königl, A., Krijt, S., & Ciesla, F. J. 2019, *ApJ*, 882, 33, doi: [10.3847/1538-4357/ab311a](https://doi.org/10.3847/1538-4357/ab311a)
- Giorgini, J. D., Yeomans, D. K., Chamberlin, A. B., et al. 1996, in *AAS/Division for Planetary Sciences Meeting Abstracts #28, AAS/Division for Planetary Sciences Meeting Abstracts*, 25.04
- Gulbis, A. A. S., Bus, S. J., Elliot, J. L., et al. 2011, *PASP*, 123, 461, doi: [10.1086/659636](https://doi.org/10.1086/659636)
- Güttler, C., Mannel, T., Rotundi, A., et al. 2019, *A&A*, 630, A24, doi: [10.1051/0004-6361/201834751](https://doi.org/10.1051/0004-6361/201834751)
- Hackwell, J. A., Warren, D. W., Chatelain, M. A., et al. 1990, *Society of Photo-Optical Instrumentation Engineers (SPIE) Conference Series*, Vol. 1235, *Low-resolution array spectrograph for the 2.9- to 13.5-um spectral region*, ed. D. L. Crawford, 171–180, doi: [10.1117/12.19086](https://doi.org/10.1117/12.19086)

- Hadamcik, E., Lasue, J., Levasseur-Regourd, A. C., & Renard, J. B. 2020, *Planet. Space Sci.*, 183, 104527, doi: [10.1016/j.pss.2018.04.022](https://doi.org/10.1016/j.pss.2018.04.022)
- Hanner, M. S. 1983, in *Cometary Exploration*, Volume 2, Vol. 2, 1–22
- Hanner, M. S., Lynch, D. K., & Russell, R. W. 1994, *ApJ*, 425, 274, doi: [10.1086/173984](https://doi.org/10.1086/173984)
- Hanner, M. S., & Zolensky, M. E. 2010, *The Mineralogy of Cometary Dust*, ed. T. Henning, Vol. 815, 203–232, doi: [10.1007/978-3-642-13259-9_4](https://doi.org/10.1007/978-3-642-13259-9_4)
- Hanner, M. S., Gehrz, R. D., Harker, D. E., et al. 1997, *Earth Moon and Planets*, 79, 247, doi: [10.1023/A:1006201820477](https://doi.org/10.1023/A:1006201820477)
- Harker, D. E., & Desch, S. J. 2002, *ApJL*, 565, L109, doi: [10.1086/339363](https://doi.org/10.1086/339363)
- Harker, D. E., Wooden, D. H., Woodward, C. E., & Lisse, C. M. 2002, *ApJ*, 580, 579, doi: [10.1086/343091](https://doi.org/10.1086/343091)
- Harker, D. E., Woodward, C. E., Kelley, M. S., et al. 2011, *AJ*, 141, 26, doi: [10.1088/0004-6256/141/1/26](https://doi.org/10.1088/0004-6256/141/1/26)
- Harker, D. E., Woodward, C. E., Kelley, M. S. P., et al. 2017, *AJ*, 153, 49, doi: [10.3847/1538-3881/153/1/49](https://doi.org/10.3847/1538-3881/153/1/49)
- Harker, D. E., Woodward, C. E., Kelley, M. S. P., & Wooden, D. H. 2018, *AJ*, 155, 199, doi: [10.3847/1538-3881/aab778](https://doi.org/10.3847/1538-3881/aab778)
- Harker, D. E., Woodward, C. E., Wooden, D. H., Fisher, R. S., & Trujillo, C. A. 2007, *Icarus*, 190, 432, doi: [10.1016/j.icarus.2007.03.008](https://doi.org/10.1016/j.icarus.2007.03.008)
- Hendrix, A. R., Vilas, F., & Li, J.-Y. 2016, *Meteoritics and Planetary Science*, 51, 105, doi: [10.1111/maps.12575](https://doi.org/10.1111/maps.12575)
- Herique, A., Kofman, W., Beck, P., et al. 2016, *MNRAS*, 462, S516, doi: [10.1093/mnras/stx040](https://doi.org/10.1093/mnras/stx040)
- Herter, T. L., Adams, J. D., Gull, G. E., et al. 2018, *Journal of Astronomical Instrumentation*, 7, 1840005, doi: [10.1142/S2251171718400056](https://doi.org/10.1142/S2251171718400056)
- Hornung, K., Merouane, S., Hilchenbach, M., et al. 2016, *Planet. Space Sci.*, 133, 63, doi: [10.1016/j.pss.2016.07.003](https://doi.org/10.1016/j.pss.2016.07.003)
- Hughes, A. L. H., & Armitage, P. J. 2010, *ApJ*, 719, 1633, doi: [10.1088/0004-637X/719/2/1633](https://doi.org/10.1088/0004-637X/719/2/1633)
- Hyland, M. G., Fitzsimmons, A., & Snodgrass, C. 2019, *MNRAS*, 484, 1347, doi: [10.1093/mnras/stz075](https://doi.org/10.1093/mnras/stz075)
- Ishii, H. A., Bradley, J. P., Bechtel, H. A., et al. 2018, *Proceedings of the National Academy of Science*, 115, 6608, doi: [10.1073/pnas.1720167115](https://doi.org/10.1073/pnas.1720167115)
- Jacquet, E. 2014, *Icarus*, 232, 176, doi: [10.1016/j.icarus.2014.01.012](https://doi.org/10.1016/j.icarus.2014.01.012)
- Jaeger, C., Molster, F. J., Dorschner, J., et al. 1998, *A&A*, 339, 904
- Jäger, C., Sabri, T., Wendler, E., & Henning, T. 2016, *ApJ*, 831, 66, doi: [10.3847/0004-637X/831/1/66](https://doi.org/10.3847/0004-637X/831/1/66)
- Jones, A. P. 2016, *Royal Society Open Science*, 3, 160224, doi: [10.1098/rsos.160224](https://doi.org/10.1098/rsos.160224)
- Jones, A. P., Köhler, M., Ysard, N., Bocchio, M., & Verstraete, L. 2017, *A&A*, 602, A46, doi: [10.1051/0004-6361/201630225](https://doi.org/10.1051/0004-6361/201630225)
- Jones, A. P., & Ysard, N. 2019, *A&A*, 627, A38, doi: [10.1051/0004-6361/201935532](https://doi.org/10.1051/0004-6361/201935532)
- Jost, B., Pommerol, A., Poch, O., et al. 2017, *Planet. Space Sci.*, 148, 1, doi: [10.1016/j.pss.2017.09.009](https://doi.org/10.1016/j.pss.2017.09.009)
- Joswiak, D. J., Brownlee, D. E., Nguyen, A. N., & Messenger, S. 2017, *Meteoritics and Planetary Science*, 52, 1612, doi: [10.1111/maps.12877](https://doi.org/10.1111/maps.12877)
- Joswiak, D. J., Nakashima, D., Brownlee, D. E., et al. 2014, *GeoCoA*, 144, 277, doi: [10.1016/j.gca.2014.08.017](https://doi.org/10.1016/j.gca.2014.08.017)
- Keller, L. P., & Messenger, S. 2011, *GeoCoA*, 75, 5336, doi: [10.1016/j.gca.2011.06.040](https://doi.org/10.1016/j.gca.2011.06.040)
- Keller, L. P., Messenger, S., Flynn, G. J., et al. 2004, *GeoCoA*, 68, 2577, doi: [10.1016/j.gca.2003.10.044](https://doi.org/10.1016/j.gca.2003.10.044)
- Keller, L. P., Hony, S., Bradley, J. P., et al. 2002, *Nature*, 417, 148, doi: [10.1038/417148a](https://doi.org/10.1038/417148a)
- Kelley, M. S., Woodward, C. E., Harker, D. E., et al. 2006, *ApJ*, 651, 1256, doi: [10.1086/507701](https://doi.org/10.1086/507701)
- Kelley, M. S., Fernández, Y. R., Licandro, J., et al. 2013, *Icarus*, 225, 475, doi: [10.1016/j.icarus.2013.04.012](https://doi.org/10.1016/j.icarus.2013.04.012)
- Kemper, F., Vriend, W. J., & Tielens, A. G. G. M. 2004, *ApJ*, 609, 826, doi: [10.1086/421339](https://doi.org/10.1086/421339)
- Klarmann, L., Ormel, C. W., & Dominik, C. 2018, *A&A*, 618, L1, doi: [10.1051/0004-6361/201833719](https://doi.org/10.1051/0004-6361/201833719)
- Koike, C., Imai, Y., Chihara, H., et al. 2010, *ApJ*, 709, 983, doi: [10.1088/0004-637X/709/2/983](https://doi.org/10.1088/0004-637X/709/2/983)
- Koike, C., Noguchi, R., Chihara, H., et al. 2013, *ApJ*, 778, 60, doi: [10.1088/0004-637X/778/1/60](https://doi.org/10.1088/0004-637X/778/1/60)
- Kolokolova, L., Kimura, H., Kiselev, N., & Rosenbush, V. 2007, *A&A*, 463, 1189, doi: [10.1051/0004-6361:20065069](https://doi.org/10.1051/0004-6361:20065069)
- Kracher, A., Scott, E. R. D., & Keil, K. 1984, *Lunar and Planetary Science Conference Proceedings*, 89, B559, doi: [10.1029/JB089iS02p0B559](https://doi.org/10.1029/JB089iS02p0B559)
- Kwon, Y. G., Ishiguro, M., Kuroda, D., et al. 2017, *AJ*, 154, 173, doi: [10.3847/1538-3881/aa89ef](https://doi.org/10.3847/1538-3881/aa89ef)
- Laher, R. R., Gorjian, V., Rebull, L. M., et al. 2012, *PASP*, 124, 737, doi: [10.1086/666883](https://doi.org/10.1086/666883)
- Langevin, Y., Hilchenbach, M., Vincendon, M., et al. 2017, *MNRAS*, 469, S535, doi: [10.1093/mnras/stx2070](https://doi.org/10.1093/mnras/stx2070)
- Langevin, Y., Merouane, S., Hilchenbach, M., et al. 2020, *Planet. Space Sci.*, 182, 104815, doi: [10.1016/j.pss.2019.104815](https://doi.org/10.1016/j.pss.2019.104815)
- Lantz, C., Brunetto, R., Barucci, M. A., et al. 2015, *A&A*, 577, A41, doi: [10.1051/0004-6361/201425398](https://doi.org/10.1051/0004-6361/201425398)
- Lee, J.-E., Bergin, E. A., & Nomura, H. 2010, *ApJL*, 710, L21, doi: [10.1088/2041-8205/710/1/L21](https://doi.org/10.1088/2041-8205/710/1/L21)

- Lindsay, S. S., Wooden, D. H., Harker, D. E., et al. 2013, *ApJ*, 766, 54, doi: [10.1088/0004-637X/766/1/54](https://doi.org/10.1088/0004-637X/766/1/54)
- Lisse, C. M., A'Hearn, M. F., Hauser, M. G., et al. 1998, *ApJ*, 496, 971, doi: [10.1086/305397](https://doi.org/10.1086/305397)
- Lisse, C. M., A'Hearn, M. F., Groussin, O., et al. 2005, *ApJL*, 625, L139, doi: [10.1086/431238](https://doi.org/10.1086/431238)
- Lodders, K. 2010, *Astrophysics and Space Science Proceedings*, 16, 379, doi: [10.1007/978-3-642-10352-0_8](https://doi.org/10.1007/978-3-642-10352-0_8)
- Lyra, W., & Umurhan, O. M. 2019, *PASP*, 131, 072001, doi: [10.1088/1538-3873/aaf5ff](https://doi.org/10.1088/1538-3873/aaf5ff)
- Marcus, J. N. 2007a, *International Comet Quarterly*, 29, 119
- . 2007b, *International Comet Quarterly*, 29, 39
- Marschall, R., Markkanen, J., Gerig, S.-B., et al. 2020, arXiv e-prints, arXiv:2005.13700, <https://arxiv.org/abs/2005.13700>
- Mathurin, J., Dartois, E., Pino, T., et al. 2019, *A&A*, 622, A160, doi: [10.1051/0004-6361/201833957](https://doi.org/10.1051/0004-6361/201833957)
- Matrajt, G., Flynn, G., Brownlee, D., Joswiak, D., & Bajt, S. 2013, *ApJ*, 765, 145, doi: [10.1088/0004-637X/765/2/145](https://doi.org/10.1088/0004-637X/765/2/145)
- Matrajt, G., Messenger, S., Ito, M., Joswiak, D., & Brownlee, D. 2008a, *Geochimica et Cosmochimica Acta Supplement*, 72, A603
- Matrajt, G., Muñoz Caro, G. M., Dartois, E., et al. 2005, *A&A*, 433, 979, doi: [10.1051/0004-6361:20041605](https://doi.org/10.1051/0004-6361:20041605)
- Matrajt, G., Ito, M., Wirick, S., et al. 2008b, *Meteoritics and Planetary Science*, 43, 315, doi: [10.1111/j.1945-5100.2008.tb00625.x](https://doi.org/10.1111/j.1945-5100.2008.tb00625.x)
- McCauley, P. I., Saar, S. H., Raymond, J. C., Ko, Y.-K., & Saint-Hilaire, P. 2013, *ApJ*, 768, 161, doi: [10.1088/0004-637X/768/2/161](https://doi.org/10.1088/0004-637X/768/2/161)
- Meech, K. J., Pittichová, J., Bar-Nun, A., et al. 2009, *Icarus*, 201, 719, doi: [10.1016/j.icarus.2008.12.045](https://doi.org/10.1016/j.icarus.2008.12.045)
- Merouane, S., Djouadi, Z., & Le Sergeant d'Hendecourt, L. 2014, *ApJ*, 780, 174, doi: [10.1088/0004-637X/780/2/174](https://doi.org/10.1088/0004-637X/780/2/174)
- Merouane, S., Zaprudin, B., Stenzel, O., et al. 2016, *A&A*, 596, A87, doi: [10.1051/0004-6361/201527958](https://doi.org/10.1051/0004-6361/201527958)
- Messenger, S., Nakamura-Messenger, K., & Keller, L. P. 2008, in *Lunar and Planetary Science Conference, Lunar and Planetary Science Conference*, 2391
- Min, M., Hovenier, J. W., de Koter, A., Waters, L. B. F. M., & Dominik, C. 2005, *Icarus*, 179, 158, doi: [10.1016/j.icarus.2005.05.015](https://doi.org/10.1016/j.icarus.2005.05.015)
- Misener, W., Krijt, S., & Ciesla, F. J. 2019, *ApJ*, 885, 118, doi: [10.3847/1538-4357/ab4a13](https://doi.org/10.3847/1538-4357/ab4a13)
- Moroz, L., Baratta, G., Strazzulla, G., et al. 2004, *Icarus*, 170, 214, doi: [10.1016/j.icarus.2004.02.003](https://doi.org/10.1016/j.icarus.2004.02.003)
- Nanne, J. A. M., Nimmo, F., Cuzzi, J. N., & Kleine, T. 2019, *Earth and Planetary Science Letters*, 511, 44, doi: [10.1016/j.epsl.2019.01.027](https://doi.org/10.1016/j.epsl.2019.01.027)
- Oort, J. H. 1950, *BAN*, 11, 91
- Pfeil, T., & Klahr, H. 2019, *ApJ*, 871, 150, doi: [10.3847/1538-4357/aaf962](https://doi.org/10.3847/1538-4357/aaf962)
- . 2020, arXiv e-prints, arXiv:2008.11195, <https://arxiv.org/abs/2008.11195>
- Pfüller, E., Wiedemann, M., Wolf, J., & Krabbe, A. 2016, *Society of Photo-Optical Instrumentation Engineers (SPIE) Conference Series*, Vol. 9908, Development of the FPI+ as facility science instrument for SOFIA cycle four observations, 99082W, doi: [10.1117/12.2233490](https://doi.org/10.1117/12.2233490)
- Poch, O., Istiqomah, I., Quirico, E., et al. 2020, *Science*, 367, aaw7462, doi: [10.1126/science.aaw7462](https://doi.org/10.1126/science.aaw7462)
- Possolo, A., Merktas, C., & Bodnar, O. 2019, *Metrologia*, 56, 045009, doi: [10.1088/1681-7575/ab2a8d](https://doi.org/10.1088/1681-7575/ab2a8d)
- Poulet, F., Lucchetti, A., Bibring, J. P., et al. 2016, *MNRAS*, 462, S23, doi: [10.1093/mnras/stw1959](https://doi.org/10.1093/mnras/stw1959)
- Powell, D., Murray-Clay, R., Pérez, L. M., Schlichting, H. E., & Rosenthal, M. 2019, *ApJ*, 878, 116, doi: [10.3847/1538-4357/ab20ce](https://doi.org/10.3847/1538-4357/ab20ce)
- Protopapa, S., Kelley, M. S. P., Yang, B., et al. 2018, *ApJL*, 862, L16, doi: [10.3847/2041-8213/aad33b](https://doi.org/10.3847/2041-8213/aad33b)
- Quirico, E., Moroz, L. V., Schmitt, B., et al. 2016, *Icarus*, 272, 32, doi: [10.1016/j.icarus.2016.02.028](https://doi.org/10.1016/j.icarus.2016.02.028)
- Raponi, A., Ciarniello, M., Capaccioni, F., et al. 2020, *Nature Astronomy*, 4, 500, doi: [10.1038/s41550-019-0992-8](https://doi.org/10.1038/s41550-019-0992-8)
- Rinaldi, G., Della Corte, V., Fulle, M., et al. 2017, *MNRAS*, 469, S598, doi: [10.1093/mnras/stx1873](https://doi.org/10.1093/mnras/stx1873)
- Rinaldi, G., Bockelée-Morvan, D., Ciarniello, M., et al. 2018, *MNRAS*, 481, 1235, doi: [10.1093/mnras/sty2266](https://doi.org/10.1093/mnras/sty2266)
- Robertson, J. 2002, *Materials Science and Engineering: R: Reports*, 37, 129, doi: [https://doi.org/10.1016/S0927-796X\(02\)00005-0](https://doi.org/10.1016/S0927-796X(02)00005-0)
- Roush, T., Pollack, J., & Orenberg, J. 1991, *Icarus*, 94, 191, doi: [10.1016/0019-1035\(91\)90150-R](https://doi.org/10.1016/0019-1035(91)90150-R)
- Rubin, M., Engrand, C., Snodgrass, C., et al. 2020, *SSRv*, 216, 102, doi: [10.1007/s11214-020-00718-2](https://doi.org/10.1007/s11214-020-00718-2)
- Ruzicka, A. M., Hutson, M., Friedrich, J. M., et al. 2017, *Meteoritics and Planetary Science*, 52, 1963, doi: [10.1111/maps.12901](https://doi.org/10.1111/maps.12901)
- Samarasinha, N., Martin, P., & Larson, S. 2014, in *Asteroids, Comets, Meteors 2014*, ed. K. Muinonen, A. Penttilä, M. Granvik, A. Virkki, G. Fedorets, O. Wilkman, & T. Kohout, 462
- Samarasinha, N. H., & Larson, S. M. 2014, *Icarus*, 239, 168, doi: [10.1016/j.icarus.2014.05.028](https://doi.org/10.1016/j.icarus.2014.05.028)

- Schambeau, C. A., Fernández, Y. R., Lisse, C. M., Samarasinha, N., & Woodney, L. M. 2015, *Icarus*, 260, 60, doi: [10.1016/j.icarus.2015.06.038](https://doi.org/10.1016/j.icarus.2015.06.038)
- Schleicher, D. G., Millis, R. L., & Birch, P. V. 1998, *Icarus*, 132, 397, doi: [10.1006/icar.1997.5902](https://doi.org/10.1006/icar.1997.5902)
- Sengupta, D. 2019, PhD thesis, University of Delaware
- Sitko, M., Russell, R., & Yanamandra-Fisher, P. 2013, in European Planetary Science Congress, EPSC2013-524
- Sitko, M. L., Lynch, D. K., Russell, R. W., & Hanner, M. S. 2004, *ApJ*, 612, 576, doi: [10.1086/421991](https://doi.org/10.1086/421991)
- Sprague, A. L., Emery, J. P., Donaldson, K. L., et al. 2002, *Meteoritics and Planetary Science*, 37, 1255, doi: [10.1111/j.1945-5100.2002.tb00894.x](https://doi.org/10.1111/j.1945-5100.2002.tb00894.x)
- Sterken, V. J., Westphal, A. J., Altobelli, N., Malaspina, D., & Postberg, F. 2019, *SSRv*, 215, 43, doi: [10.1007/s11214-019-0607-9](https://doi.org/10.1007/s11214-019-0607-9)
- Stoll, M. H. R., Kley, W., & Picogna, G. 2017, *A&A*, 599, L6, doi: [10.1051/0004-6361/201630226](https://doi.org/10.1051/0004-6361/201630226)
- Strazzulla, G., Cooper, J. F., Christian, E. R., & Johnson, R. E. 2003, *Comptes Rendus Physique*, 4, 791, doi: [10.1016/j.crhy.2003.10.009](https://doi.org/10.1016/j.crhy.2003.10.009)
- Stroud, R. M., Lagos, M., & Batson, P. E. 2019, in Lunar and Planetary Science Conference, Lunar and Planetary Science Conference, 2259
- Sugita, S., Ootsubo, T., Kadono, T., et al. 2005, *Science*, 310, 274, doi: [10.1126/science.1119091](https://doi.org/10.1126/science.1119091)
- Swings, P. 1956, *Vistas in Astronomy*, 2, 958, doi: [10.1016/0083-6656\(56\)90020-4](https://doi.org/10.1016/0083-6656(56)90020-4)
- Teague, R., Bae, J., & Bergin, E. A. 2019, *Nature*, 574, 378, doi: [10.1038/s41586-019-1642-0](https://doi.org/10.1038/s41586-019-1642-0)
- Thomas, K. L., Blanford, G. E., Keller, L. P., Klock, W., & McKay, D. S. 1993a, *GeoCoA*, 57, 1551, doi: [10.1016/0016-7037\(93\)90012-L](https://doi.org/10.1016/0016-7037(93)90012-L)
- Thomas, K. L., Klock, W., Keller, L. P., Blanford, G. E., & McKay, D. S. 1993b, *Meteoritics*, 28, 448
- Tody, D. 1986, Society of Photo-Optical Instrumentation Engineers (SPIE) Conference Series, Vol. 627, The IRAF Data Reduction and Analysis System, ed. D. L. Crawford, 733, doi: [10.1117/12.968154](https://doi.org/10.1117/12.968154)
- . 1993, Astronomical Society of the Pacific Conference Series, Vol. 52, IRAF in the Nineties, ed. R. J. Hanisch, R. J. V. Brissenden, & J. Barnes, 173
- Tozzi, G. P., Lara, L. M., Kolokolova, L., et al. 2004, *A&A*, 424, 325, doi: [10.1051/0004-6361:20035893](https://doi.org/10.1051/0004-6361:20035893)
- Tucker, D. L., Kent, S., Richmond, M. W., et al. 2006, *Astronomische Nachrichten*, 327, 821, doi: [10.1002/asna.200610655](https://doi.org/10.1002/asna.200610655)
- Vokrouhlický, D., Nesvorný, D., & Dones, L. 2019, *AJ*, 157, 181, doi: [10.3847/1538-3881/ab13aa](https://doi.org/10.3847/1538-3881/ab13aa)
- Wehrstedt, M., & Gail, H.-P. 2008, arXiv e-prints, arXiv:0804.3377. <https://arxiv.org/abs/0804.3377>
- Wei, C.-E., Nomura, H., Lee, J.-E., et al. 2019, *ApJ*, 870, 129, doi: [10.3847/1538-4357/aaf390](https://doi.org/10.3847/1538-4357/aaf390)
- Westphal, A. J., Bridges, J. C., Brownlee, D. E., et al. 2017, *Meteoritics and Planetary Science*, 52, 1859, doi: [10.1111/maps.12893](https://doi.org/10.1111/maps.12893)
- Williams, G. V. 2019, Minor Planet Electronic Circulars, 2019-J142
- Williams, M. W., & Arakawa, E. T. 1972, *Journal of Applied Physics*, 43, 3460, doi: [10.1063/1.1661738](https://doi.org/10.1063/1.1661738)
- Wirick, S., Flynn, G. J., Keller, L. P., et al. 2009, *Meteoritics and Planetary Science*, 44, 1611, doi: [10.1111/j.1945-5100.2009.tb01194.x](https://doi.org/10.1111/j.1945-5100.2009.tb01194.x)
- Wooden, D., Desch, S., Harker, D., Gail, H. P., & Keller, L. 2007, in *Protostars and Planets V*, ed. B. Reipurth, D. Jewitt, & K. Keil, 815
- Wooden, D. H. 2002, *Earth Moon and Planets*, 89, 247, doi: [10.1023/A:1021515023679](https://doi.org/10.1023/A:1021515023679)
- . 2008, *SSRv*, 138, 75, doi: [10.1007/s11214-008-9424-2](https://doi.org/10.1007/s11214-008-9424-2)
- Wooden, D. H., Butner, H. M., Harker, D. E., & Woodward, C. E. 2000, *Icarus*, 143, 126, doi: [10.1006/icar.1999.6240](https://doi.org/10.1006/icar.1999.6240)
- Wooden, D. H., Ishii, H. A., & Zolensky, M. E. 2017, *Philosophical Transactions of the Royal Society of London Series A*, 375, 20160260, doi: [10.1098/rsta.2016.0260](https://doi.org/10.1098/rsta.2016.0260)
- Wooden, D. H., Woodward, C. E., & Harker, D. E. 2004, *ApJL*, 612, L77, doi: [10.1086/424593](https://doi.org/10.1086/424593)
- Woodward, C. E., Kelley, M. S. P., Harker, D. E., & Wooden, D. H. 2020, *ApJ*, in prep., 000, doi: [10.1088/0000-0000/000/0/000](https://doi.org/10.1088/0000-0000/000/0/000)
- Woodward, C. E., Jones, T. J., Brown, B., et al. 2011, *AJ*, 141, 181, doi: [10.1088/0004-6256/141/6/181](https://doi.org/10.1088/0004-6256/141/6/181)
- Woodward, C. E., Kelley, M. S. P., Harker, D. E., et al. 2015, *ApJ*, 809, 181, doi: [10.1088/0004-637X/809/2/181](https://doi.org/10.1088/0004-637X/809/2/181)
- Wozniakiewicz, P. J., Bradley, J. P., Ishii, H. A., et al. 2012, *ApJL*, 760, L23, doi: [10.1088/2041-8205/760/2/L23](https://doi.org/10.1088/2041-8205/760/2/L23)
- Wozniakiewicz, P. J., Bradley, J. P., Ishii, H. A., Price, M. C., & Brownlee, D. E. 2013, *ApJ*, 779, 164, doi: [10.1088/0004-637X/779/2/164](https://doi.org/10.1088/0004-637X/779/2/164)
- Xing, Z., & Hanner, M. S. 1997, *A&A*, 324, 805
- Yang, B., Jewitt, D., & Bus, S. J. 2009, *AJ*, 137, 4538, doi: [10.1088/0004-6256/137/5/4538](https://doi.org/10.1088/0004-6256/137/5/4538)
- Young, E. T., Becklin, E. E., Marcum, P. M., et al. 2012, *ApJL*, 749, L17, doi: [10.1088/2041-8205/749/2/L17](https://doi.org/10.1088/2041-8205/749/2/L17)
- Zolensky, M., & Barrett, R. 1992, *Meteoritics*, 27, 312
- Zolensky, M. E., Zega, T. J., Yano, H., et al. 2006, *Science*, 314, 1735, doi: [10.1126/science.1135842](https://doi.org/10.1126/science.1135842)